Research paper

Mixing of inclined dense jets in stationary ambient

Chris C.K. Lai [a], Joseph H.W. Lee [b,*]

[a] Department of Civil Engineering, The University of Hong Kong, Pokfulam, Hong Kong, China
[b] Department of Civil and Environmental Engineering, Hong Kong University of Science and Technology, Clear Water Bay, Hong Kong, China

Abstract

This paper reports results of a comprehensive experimental investigation of inclined round dense jets in an otherwise stagnant fluid. The tracer concentration field is measured for six jet discharge angles: $\theta_o = (15°, 30°, 38°, 45°, 52°, \& 60°)$ and jet densimetric Froude number of $Fr = 10–40$ using the planar laser-induced fluorescence (LIF) technique; selected jet velocity measurements are made using Particle Image Velocimetry (PIV). The detailed jet mixing characteristics and turbulence properties are presented. The direct velocity measurement reveals that the mixing is jet-like until the maximum rise. Empirical correlations for the maximum jet rise height, jet dilution at maximum rise, and impact dilution are presented. Both the time-mean concentration and intermittency show that the upper jet edge spreading is similar to a positively buoyant jet; at the lower edge the buoyant instability induces significant detrainment and mass outflux for $\theta_o > 15°$. The dimensionless maximum rise height $Z_{max}/(FrD)$ is independent of source conditions for $Fr \geq 25$, and varies from 0.44 for $\theta_o = 15°$ to 2.08 for $\theta_o = 60°$. Dilution measurements at terminal rise show the difference in dilution is small for $\theta_o = 38°–60°$ and the asymptotic dilution constant is $S_t/Fr = 0.45$. The impact dilution S_i is also not sensitive to jet angle for $\theta_o = 38°–60°$ and can be expressed as $S_i/Fr = 1.06$ for $Fr \geq 20$.

The Lagrangian jet model VISJET is used to interpret the experimental results. A detailed derivation for a general formulation of the entrainment coefficient is presented. Despite the observed detrainment, the trajectory and dilution are reasonably predicted; the maximum jet rise is generally under-predicted by $10–15\%$ and associated dilution by 30%. However, the predicted variation of jet behavior with discharge angle is in good agreement with measurements. The experimental data is also compared with predictions of alternative models that employ an *ad hoc* entrainment hypothesis.

1. Introduction

Wastewater effluents with a density higher than that of the environment are often discharged into coastal waters in the form of submerged dense (negatively buoyant) jets. Examples include brine discharges from desalination plants and cooling water discharges from liquefied natural gas (LNG) plants. In particular, large-scale desalination plants ($10^5–10^6$ m^3/d) have been built or planned (e.g. Singapore and Adelaide,

Australia) to cope with water scarcity caused by a growing population and climate change. The desalination process results in a concentrated brine solution that has to be properly disposed. Typically, the concentrated brine is discharged upwards in the form of inclined dense jets from a submarine multiport diffuser located on the sea bed. As the brine discharge is denser than the surrounding seawater, the jet will eventually fall back onto the sea floor where it continues to spread horizontally as a bottom density current. Environmental impact of brine discharges is of significant concern, as elevated salinity level is known to inhibit growth of marine species and may lead to the reduction of fish cultures (Milione and Zeng, 2008). It is necessary to achieve rapid mixing of the

* Corresponding author. Tel.: +86 852 2358 6161.
E-mail addresses: chrislck@hku.hk (C.C.K. Lai), hreclhw@hkucc.hku.hk, jhwlee@ust.hk (J.H.W. Lee).

brine discharge both to minimize the impact on the marine environment (e.g. sea bed ecology) and to prevent the recirculation of brine into the seawater intake. The prediction of the mixing of dense jets is necessary for outfall design and environmental impact assessment.

Compared to positively buoyant wastewater discharges, the dense jet if discharged upwards has a distinct feature in that the jet structure disintegrates at a certain elevation above the discharge. In earlier studies, it is shown (Abraham, 1967) that for a vertical dense jet there exist two zones of entrainment; an integral jet model was developed and the predicted terminal rise is in good agreement with experiments. The vertical dense jet in stagnant water tends to fall back on the source which results in significant impairment of the jet dilution; this could be prevented by inclining the jet at a small angle from the vertical (e.g. Fischer et al. (1979)). Many studies have been performed for the inclined dense jet. Zeitoun et al. (1970) used point-based conductivity technique to measure trajectory and minimum dilution of 30°, 45° and 60° jets; based on the dilution measurement the 60° jet was recommended as the optimal discharge angle. Roberts and Toms (1987) reported point-based conductivity measurements of the 60° and vertical jets. Empirical correlations of the dilution at maximum jet rise and impact on the sea floor are obtained; the data show that the 60° jet has twice the dilution of the vertical jet at both the terminal rise and impact points (Roberts and Toms (1987)).

Previous research has been directed to determine the optimal angle for a given discharge. Cipollina et al. (2005) obtained visual trajectory measurements for 30°, 45° and 60° jets primarily at high jet densimetric Froude number Fr ($Fr = 30-120$); however no dilution data are available. Kikkert et al. (2007) reported laterally integrated concentration measurements of 15°, 30°, 45° and 60° jets in stagnant water based on a light attenuation technique. A semi-analytical model was developed to interpret the results which can be separated into either a pure jet or plume regime. The comparison of the model results with previous data is satisfactory especially on the jet trajectory and suggests that dense jets are jet-like before terminal rise. The integrated dilution (averaged normal to the jet trajectory) shows the normalized dilution at terminal rise is about the same for $\theta_o = 30°-60°$. This finding is contrary to an earlier recommendation by Zeitoun et al. (1970), but is however supported by predictions of the CORJET model (Jirka, 2004, 2008) — which shows that the dilution at maximum height of rise is approximately the same for $\theta_o = 30°-60°$, with the 45° jet having a slightly higher value. In fact, Cederwall (1968) had earlier commented that the 45° angle is optimal in stationary water. However, the data in the literature are either non-existent or inconclusive (due to limited parameter range or inadequate measurements) to resolve this issue; there have also been scant measurements on the turbulence properties. A comprehensive investigation on the mixing behavior of inclined dense jets over a wide range of discharge angles is relevant for Asian coastal cities where the typically shallow depth (10—20 m) may impose restriction on the choice of jet angle that would achieve total submergence of the waste effluent below the water surface. For example, experiments have shown that the terminal rise of 45°

and 30° jets are 25% and 50% less than that of the 60° jet respectively (e.g. Cipollina et al., 2005; Lai, 2010). Very recently visual measurements of jet trajectory have been made for inclined jets with $\theta_o = 45°-90°$ (Papakostantis et al. (2011a)). Measurements of turbulent concentration fluctuation C_{rms} across a dense jet have been reported for jet angles $\theta_o = 45°, 60°$ and 75° (Papakostantis et al. (2011b)). Shao and Law (2010) also conducted combined planar LIF and PIV measurements of 30° and 45° jets.

For an inclined dense jet discharging upwards, the initial jet momentum flux is in opposite direction to the buoyancy flux; the fluid density in the lower half of the jet decreases from the jet center toward the jet edge. A fluid parcel in the lower half of the jet hence tends to descend and eventually falls off the jet when the descending velocity exceeds the entrainment velocity. This buoyancy-driven instability and the associated downflow of jet fluid are termed as detrainment or detrained flow (e.g. Kikkert et al., 2007). Such phenomenon also occurs in the upper half of a positively buoyant jet that is discharged downwards — a mirror image of the dense jet flow (e.g. see experiments by Anwar, 1969). Detrainment causes additional vertical mixing with the ambient that is not accounted for by a shear entrainment hypothesis. However, the importance of the detrainment in the modeling is unanswered due to lack of concentration and velocity measurements. On the other hand, Papanicolaou et al. (2008) showed that predictions from jet integral models can be made to agree better with observations if the jet entrainment coefficient α_j is reduced from 0.057 to 0.03—0.04. However, the validity of such an artificial reduction and the connection with the detrainment phenomenon have yet to be investigated.

This paper reports a comprehensive experimental investigation of the detailed tracer concentration field of inclined dense jets for jet densimetric Froude number of $Fr = 10-40$ and a broad range of jet angles $\theta_o = 15°, 30°, 38°, 45°, 52°$ & 60°. The theoretical framework for dimensional analysis and a general formulation for the entrainment coefficient are first presented. The experimental design and procedure are then described. Key observations are presented to elucidate the structure of a dense jet. Empirical correlations of the maximum height of rise, terminal and impact dilution as a function of jet discharge angle are discussed and compared with predictions of the VISJET model (Lee and Chu (2003)) as well as previous studies. The implications of artificial adjustment of entrainment coefficient to fit experimental data are discussed.

2. Theory

2.1. Dimensional analysis

Fig. 1 shows an inclined turbulent round dense jet ($Re > 2000$) in stationary water. The jet is discharged at an angle θ_o to the horizontal with jet diameter D, jet velocity U_j, and density $\rho_o > \rho_a$, where ρ_a is the ambient density. The jet mixes with the ambient fluid as it rises, but is decelerated by virtue of its negative buoyancy; a maximum height of rise Z_{max}
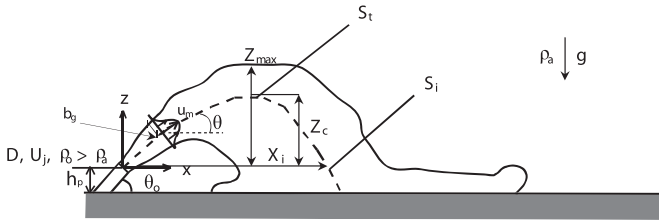
Fig. 1. An inclined round dense jet in stagnant ambient.

is reached before the jet falls over as a negatively buoyant plume to impinge on the nearby sea bed as a bottom spreading density current. The concentration field of a dense jet depends on the jet discharge concentration C_o, the initial density difference $\Delta\rho_o = \rho_o - \rho_a$, U_j, D and θ_o. In addition, the mixing behavior is affected by the complex jet impingement on the bottom and the interaction of the jet and the density current. The jet discharge densimetric Froude number, a measure of the ratio of inertia to buoyancy, can be defined as $Fr = U_j/\sqrt{g'_o D}$, where g = gravitational acceleration and $g'_o = (\Delta\rho_o/\rho_a)g$ = reduced gravitational acceleration. The jet mixing characteristics of interest are the maximum terminal rise height Z_{max} and the minimum dilution at terminal rise S_t. It is also of interest to predict the minimum "return-level" dilution S_i when the plume returns to the source level (at distance X_i from the source) and impacts on the sea bed.

The inclined dense jet discharge can be characterized by the jet discharge volume flux $Q_o = U_j\pi D^2/4$, kinematic momentum flux $M_o = U_j^2\pi D^2/4$, and buoyancy flux $B_o = Q_o g'_o$. By dimensional analysis, it can be shown that a characteristic length (e.g. maximum height of rise) for the jet trajectory can be expressed in terms of the discharge conditions as:

$$\frac{Z_{max}}{l_M} = f\left(l_M/l_Q, \theta_o\right) \tag{1}$$

or alternatively as:

$$\frac{Z_{max}}{FrD} = f(Fr, \theta_o) \tag{2}$$

where $l_M = M_o^{3/4}/B_o^{1/2}$ is a momentum length scale formed from the momentum and buoyancy fluxes, and $l_Q = Q_o/M_o^{1/2}$ is a source length scale formed from the volume and momentum fluxes. l_M is a measure of the distance within which jet momentum is more important than buoyancy, and l_Q represents the length over which source discharge is important. It should be noted that l_M and l_Q can be related to the jet diameter and densimetric Froude number as $l_M = (\pi/4)^{1/4}FrD$ and $l_Q = (\pi/4)^{1/2}D$.

The functional dependence $f(Fr, \theta_o)$ must be determined from experiments. In particular, for a given jet discharge angle θ_o, both theory and experiments have shown that $f(Fr,\theta_o)$ approaches a constant depending on θ_o for large Fr (e.g. Roberts and Toms (1987)). Similarly, the terminal level dilution (or return level dilution) can also be expressed in an analogous functional form:

$$\frac{S_t}{Fr} = g(Fr, \theta_o) \tag{3}$$

and tends to a constant $g(\theta_o)$ for large Fr.

2.2. Numerical modeling

Integral jet models have been shown to be a simple and effective method to solve jet and plume problems (e.g. Morton et al., 1956; Fischer et al., 1979). By assuming self-similarity for the boundary layer flows, the governing equations of motion for the buoyant jet can be transformed into a set of integral equations in terms of the jet volume, momentum and buoyancy fluxes. Turbulent closure can be based on either an entrainment hypothesis or a jet spreading hypothesis. Starting from the initial jet discharge conditions, the integral equations can be solved numerically, and the jet mixing characteristics can be reliably predicted to within an experimental constant (i.e. either the entrainment coefficient or jet spreading rate).

Models based on either the entrainment or jet spreading hypothesis have been successfully developed. The equivalence between these two approaches has also been established (e.g. Lee and Chu, 2003); in general, models based on the entrainment hypothesis offer more flexibility in handling general flow situations that may not strictly satisfy the basic self-similarity assumptions.

The Lagrangian model JETLAG/VISJET is employed for theoretical analysis and interpretation of the experimental results. JETLAG/VISJET is a well-proven general model that predicts the near-field mixing of an arbitrarily-inclined round buoyant jet in a stratified crossflow (Lee and Cheung, 1990; Lee et al., 2000; Lee and Chu, 2003). The unknown jet trajectory is viewed as a sequential series of plume elements which increase in mass as a result of shear entrainment (due to the jet discharge) and vortex entrainment (due to crossflow) while rising by buoyant acceleration and being sheared over by the crossflow. The model tracks the evolution of the average properties of a plume element (corresponding to a 'top-hat' profile) at each step by conservation of horizontal and vertical momentum, conservation of mass accounting for entrainment, and conservation of tracer mass/heat. In particular, the performance of the model (which incorporates a general shear entrainment hypothesis) for positively buoyant jets in stagnant fluid has been extensively validated against basic data.

2.2.1. General entrainment formulation for an inclined round buoyant jet

Employing the entrainment hypothesis, it is assumed that the turbulent entrainment is caused by velocity shear. The entrainment velocity v_e at the edge of the jet is assumed to be proportional to the local jet centerline velocity u_m, $v_e = \alpha u_m$ where α is the entrainment coefficient.

For a positively buoyant jet, it is recognized that the entrainment coefficient α is not a constant but varies with the local densimetric Froude number Fr_L; it depends on the local balance of jet buoyancy and momentum. By assuming self-

similarity of the jet flow, a general relation between α and the local jet discharge angle θ and jet densimetric Froude number Fr_L can be derived for a turbulent round buoyant jet (Appendix A), where $Fr_L = u_m / \sqrt{(\Delta\rho_m/\rho_a)gb_g}$; u_m and $\Delta\rho_m = \rho_a - \rho_m > 0$ are the centerline velocity and centerline density difference, and b_g is the nominal jet half-width (Fig. 1 and Appendix A).

As shown in Appendix A, $\alpha = f(\theta, Fr_L)$ can be expressed in the following form for both positively or negatively buoyant jets:

$$\alpha = \alpha_j + (\alpha_p - \alpha_j)\, \sin\theta\, \frac{Fr_p^2}{Fr_L^2} \qquad (4)$$

where $\alpha_j = 0.057$ and $\alpha_p = 0.085$ are the entrainment coefficient (based on Gaussian profile) for a pure jet and pure plume respectively (Lee and Chu, 2003). For a negatively buoyant jet with $\Delta\rho_m < 0$, Fr_L cannot be meaningfully defined. However, this is immaterial as the variation of α as expressed in Eq. (4) depends only on Fr_L^2. For pure jets, $\Delta\rho_m \to 0$, $Fr_L \to \infty$, and $\alpha = \alpha_j$. It can be shown that all positively buoyant jets ($Fr > 0$) tend to plumes far away from the source, and Fr_L approaches the asymptotic plume densimetric Fr_p where $Fr_p = \sqrt{5\lambda^2/4\alpha_p} = 4.6$ ($\lambda = 1.2$; Lee and Chu, 2003).

For a dense jet, $Fr_L^2 \le 0$, the second term on the R.H.S of Eq. (4) is negative. Thus, the entrainment coefficient α can be smaller than α_j. The local jet inclination θ also affects α; the buoyancy effect tends to be weaker for smaller jet discharge angles θ_o.

The general formulation (4) is incorporated in VISJET (Lee et al., 2000). The variation of α along the trajectory of a dense jet is illustrated using VISJET for a free dense jet with $Fr \approx 26$ and for 5 representative jet angles $\theta = 15, 20, 30, 45$ & $60°$. The calculations are allowed to continue as the jet falls below the source level; a bottom boundary is not simulated. Fig. 2(a) and (b) show the predicted centerline jet trajectory and the corresponding variation of entrainment coefficient respectively. It is seen that the jet rises to a maximum height of $x/(DFr) \approx 1.2-1.5$ (Fig. 2(a)); the entrainment coefficient α decreases to a minimum value before the maximum rise,

increases to α_j at terminal rise, after which it increases toward the asymptotic plume value rapidly in the descent phase. For the small discharge angles, 15° and 20°, α decreases slightly below α_j during the ascent, and increases toward the asymptotic plume value α_p during the falling phase as a negative plume. For the 45° and 60° jets (Fig. 2(a)), α drops significantly to 0.045 and 0.025 respectively before the maximum rise, after which it increases rapidly to α_p. These theoretical results offer additional insights that are useful in the interpretation of experimental data. Different variants of the general formulation including the *ad hoc* reduction of entrainment coefficient (Papanicolaou et al., 2008) are also studied by comparing the model predictions with dense jet data (Appendix B).

3. Experimental setup and procedure

Experiments were carried out in a 1.2 m wide by 11 m long flume (Fig. 3) partitioned from a 5 m by 11 m shallow water basin (not shown). The jet discharge nozzle is made from a tapering nozzle head with internal diameter that varies from 30 mm to $D = 5$ mm on exit (tapered length $= 11D$). The nozzle head is mounted onto a transparent Perspex false floor through an anchor plate with a hinge joint; the jet nozzle is fixed at an elevation of 5 cm from the floor, allowing sufficient room to avoid bottom jet attachment. Density differences are created by adding table salt to tap water. For every 5 L of fresh water, 77 g or 180 g of salt was added to create nominal initial density differences of 1.14% or 2.5% respectively. The actual density of the source fluid was measured by a Kyoto Electronic density meter (model DA-500). The jet discharge is fed from a constant-head tank; the flow rate is monitored by a calibrated Tokyo Keiso rotameter.

3.1. Laser induced fluorescence (LIF)

The tracer concentration field was measured using the Laser-induced Fluorescence (LIF) technique. Rhodamine-6G dye was added as tracer. A horizontal laser sheet (2 mm thickness) was generated from a 5 W Argon-Ion laser and
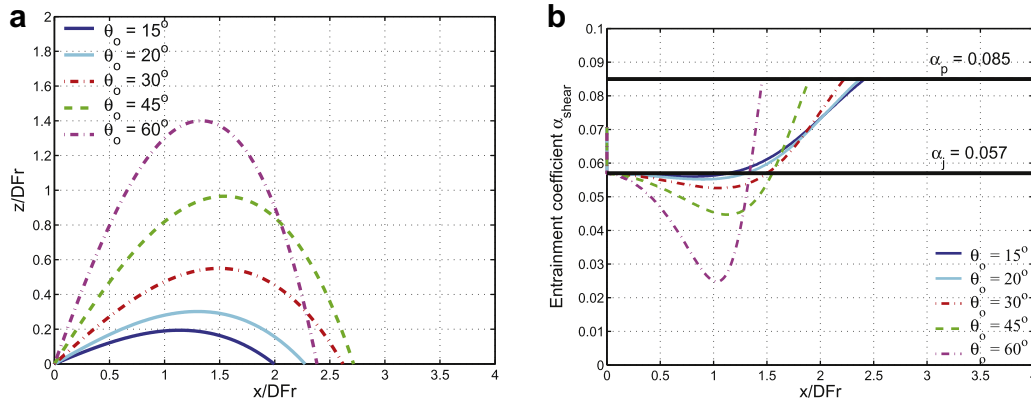
Fig. 2. Jet trajectory and variation of entrainment coefficient in an inclined dense jet ($Fr \sim 26$) as predicted by VISJET: (a) jet centerline trajectory; and (b) entrainment coefficient.
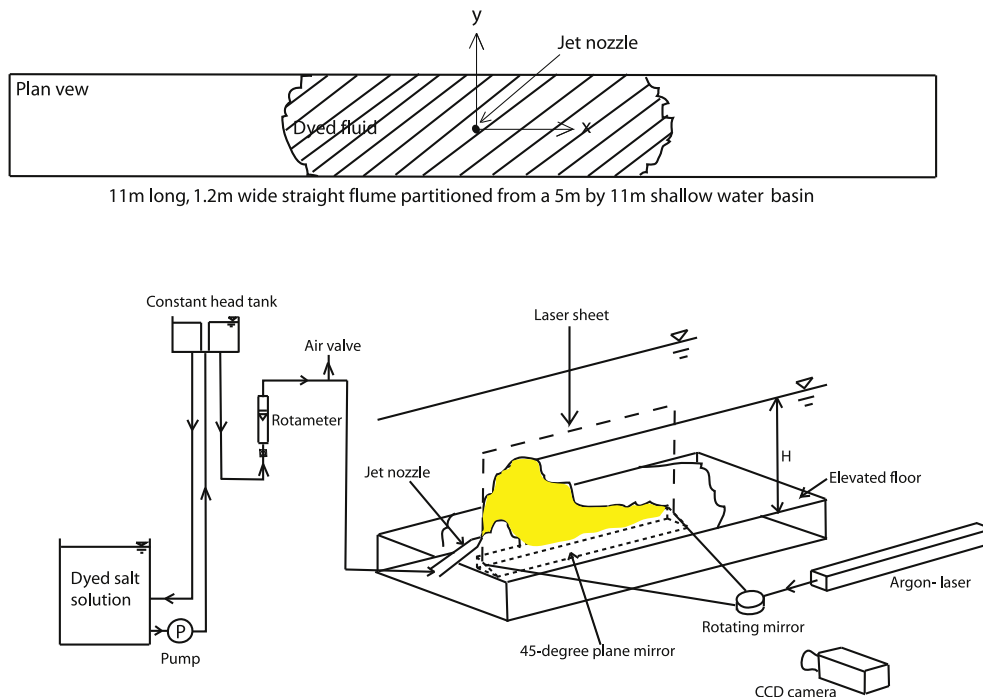
Fig. 3. Experimental setup for inclined dense jets in stagnant ambient.

a high frequency rotating mirror. This horizontal laser sheet was then made vertical by reflecting it upwards by a 45° plane mirror placed beneath the false floor. The mirror was carefully aligned such that the vertical laser sheet cut through the centerline section (plane of symmetry) of the jet. For cross-sectional planes, a vertical laser sheet was generated by the rotating mirror directly.

Depending on the desirable image size, lens of different focal lengths (24 mm, 35 mm & 60 mm) was fitted to a charge-coupled device (CCD) camera. The camera was placed 3.5 m (see Fig. 3) away from the longitudinal section of interest. This separation between the camera and test section is sufficiently large such that the effects of parallax would be insignificant. To ensure good contrast of images, a Hoya orange filter was used to filter out laser and other scattered light in the background. The camera shutter speed was set at 0.1s. The image resolution was 576 × 768 pixels and captured jet images were digitized as 8-bit grayscale bitmap files.

The amount of dye added to source fluid was carefully controlled; a too high concentration leads to significant attenuation in emitted light intensity whereas a too low concentration leads to poor contrast between jet and background. Based on past experience (Chu, 1996), dye concentrations of around 0.1 mg/L were adopted in all experiments; the highest concentration used was 0.2 mg/L.

Before the start of each experiment the area surrounding the measurement section was darkened; background images were taken for 10s. After steady flow had been established, the images of the dense jet were then captured continuously for 60s. Similar setting was used in cross-section measurements except that images were captured for 90s, giving 900 images for analysis. The jet images were time-averaged and the mean

jet image was obtained by subtracting the background. It was then used in subsequent analysis. The initial source concentration C_o was determined using a calibration box filled with source fluid placed at the measurement section and illuminated with the same laser sheet. The average light intensity, taken from one hundred images, of the entire box was taken as C_o. Samples of source fluid were collected and the density was measured. Jet discharge and ambient temperatures were measured with an electronic thermometer.

3.2. Particle Image Velocimetry (PIV)

Velocity distribution in dense jets for selected experiments was measured by a PIV system designed by *Dantec Dynamics*. The PIV system had four components; a 400 mJ Litro YAG pulse laser, an optical system, a high-speed CCD camera and a computer for synchronization between camera and lasers. The laser emitted two green laser beams at a wavelength of 532 nm and they were made to overlap to ensure correct velocity field calculation. The aligned beams then passed through the optical system, which was made up of a series of plane mirrors and a cylindrical lens, for the generation of planar laser sheets. The CCD camera had a resolution of 1024 by 1344 pixels and was synchronized with the pulse laser so that images were taken at the same time when the laser flashed. A filter which blocked light with wavelengths larger than 532 nm was added to the camera to enure the quality of images. The rest of the experimental setup was very similar to those in LIF experiments except the laser sheets were directed from overhead. Images were taken in the double frame (image) mode from which the instantaneous velocity field was calculated by cross-correlation between the two frames. The

Table 1
Experimental parameters of inclined round dense jet in stationary ambient (jet diameter $D = 5$ mm).

Jet discharge flow Q_o (L/hr)	Jet density ρ_j (g/cm^3)	Ambient density ρ_a (g/cm^3)	Jet temperature T_j (°C)	Ambient temperature T_a (°C)	Jet densimetric Froude number Fr	Jet Reynolds number Re
			Jet angle, $\theta_o = 15°$			
28.2	1.0245	0.9980	24.3	21.1	11.0	1994
47	1.0245	0.9980	24.3	21.1	18.5	3324
65.8	1.0245	0.9980	24.3	21.1	25.8	4653
84.6	1.0245	0.9980	24.3	21.1	33.2	5982
103.4	1.0245	0.9980	24.3	21.1	40.5	7639
28.2	1.0123	0.9970	25.1	25.1	14.5	1994
			$\theta_o = 30°$			
28.2	1.0254	0.9981	20.6	20.5	10.9	1994
37.6	1.0254	0.9981	20.6	20.5	14.5	2659
47	1.0254	0.9981	20.6	20.5	18.1	3324
56.4	1.0254	0.9981	20.6	20.5	21.8	3988
65.8	1.0254	0.9981	20.6	20.5	25.4	4653
75.2	1.0254	0.9981	20.6	20.5	29.1	5318
84.6	1.0254	0.9981	20.6	20.5	32.7	5982
28.2	1.0098	0.9972	26.2	24.4	16.1	1994
37.6	1.0098	0.9972	26.2	24.4	21.4	2659
47	1.0098	0.9972	26.2	24.4	26.8	3324
28.2	1.0117	0.9973	24.2	24.1	14.9	1994
			$\theta_o = 38°$			
28.2	1.0256	0.9980	23.1	20.9	10.8	1994
37.6	1.0256	0.9980	23.1	20.9	14.4	2659
47	1.0256	0.9980	23.1	20.9	18.1	3324
56.4	1.0256	0.9980	23.1	20.9	22.6	3988
65.8	1.0256	0.9980	23.1	20.9	25.2	4653
84.6	1.0256	0.9980	23.1	20.9	32.5	5982
103.4	1.0256	0.9980	23.1	20.9	39.6	7312
28.2	1.0098	0.9971	24.9	24.6	16.0	1994
37.6	1.0098	0.9971	24.9	24.6	21.3	2659
47	1.0098	0.9971	24.9	24.6	26.7	3324
			$\theta_o = 45°$			
28.2	1.021	0.9981	22.3	20.7	11.8	1994
37.6	1.021	0.9981	22.3	20.7	15.8	2659
47	1.021	0.9981	22.3	20.7	19.8	3324
56.4	1.021	0.9981	22.3	20.7	23.8	3988
65.8	1.021	0.9981	22.3	20.7	27.7	4653
75.2	1.021	0.9981	22.3	20.7	31.7	5318
84.6	1.021	0.9981	22.3	20.7	35.6	5982
94	1.021	0.9981	22.3	20.7	39.6	6647
28.2	1.0098	0.9972	25.2	24.5	16.0	1994
37.6	1.0098	0.9972	25.2	24.5	21.4	2659
47	1.0098	0.9972	25.2	24.5	26.7	3324
28.2	1.011	0.9969	25.3	25.5	15.2	1994
			$\theta_o = 52°$			
28.2	1.0241	0.9977	23.2	22.3	11.1	1994
47	1.0241	0.9977	23.2	22.3	18.5	3324
56.4	1.0241	0.9977	23.2	22.3	22.1	3988
65.8	1.0241	0.9977	23.2	22.3	25.8	4653
75.2	1.0241	0.9977	23.2	22.3	29.5	5318
84.6	1.0241	0.9977	23.2	22.3	33.2	5982
103.4	1.0241	0.9977	23.2	22.3	40.6	7312
28.2	1.0098	0.9972	26.1	24.4	16.0	1994
37.6	1.0098	0.9972	26.1	24.4	21.4	2659
47	1.0098	0.9972	26.1	24.4	26.7	3324
			$\theta_o = 60°$			
28.2	1.0241	0.9977	21.7	22.3	11.1	1994
47	1.0241	0.9977	21.7	22.3	18.5	3324
56.4	1.0241	0.9977	21.7	22.3	22.1	3988
65.8	1.0241	0.9977	21.7	22.3	25.8	4653
84.6	1.0241	0.9977	21.7	22.3	33.2	5982
94	1.0241	0.9977	21.7	22.3	36.9	6647

Table 1 (*continued*)

Jet discharge flow Q_o (L/hr)	Jet density ρ_j (g/cm^3)	Ambient density ρ_a (g/cm^3)	Jet temperature T_j (°C)	Ambient temperature T_a (°C)	Jet densimetric Froude number Fr	Jet Reynolds number Re
28.2	1.0098	0.9972	26.4	24.5	16.1	1994
37.6	1.0098	0.9972	26.4	24.5	21.4	2659
47	1.0098	0.9972	26.4	24.5	26.8	3324
28.2	1.0226	0.9977	23.1	22.5	11.4	1994
47	1.0226	0.9977	23.1	22.5	19.0	3324
65.8	1.0225	0.9977	23.8	22.5	26.6	4653
28.2	1.0188	0.9984	23.7	20.7	12.6	1994
37.6	1.0188	0.9984	24.3	20.7	16.8	2659
47	1.0188	0.9984	24.3	20.7	20.9	3324

sampling frequency was set at 5–7 Hz and images were captured continuously for 2 min, resulting in 600–700 image pairs for each experiment run.

Velocity vectors were calculated within a 16 by 16 pixels interrogation area with an overlapping ratio of 25% or 50%. Depending on the ratio, the total number of vectors generated is different; 9435 and 21,209 velocity vectors were generated correspondingly. Raw images (vector field) after correlation were subjected to a screening procedure to filter out unrealistic vectors; less than 3% of the raw vectors was filtered out. More details on the LIF and PIV techniques can be found in Lai (2010).

A summary of the experimental parameters is given in Table 1. A summary of experimental parameters and conditions of previous studies is given in Table 2.

4. Experimental results

4.1. General observations

The discharge of 15°, 30° & 60° dense jets ($Fr = 16$) are shown in Fig. 4. For $\theta_o = 15°$, the jet spreads linearly and rises to the maximum height before falling over. For the 60° jet, tracer of the jet fluid is leaving the main flow even before the entire flow field is established. The descending flow is seemingly moving backwards, resulting in a reverse flow of which the jet may re-entrain and dilution may be lowered. The jet impinges onto the false floor after 20s and starts to spread radially outward. Finally, a steady state in the near-field is attained at around 30s. From this time onwards, flow reversal

observed at the beginning is absent. Detrained jet fluid begins to fall at small distances from source and it moves predominantly in the forward horizontal direction. The inner (lower) edge is blurred when compared to the outer (upper) edge. The detrained flow destroys the axis-symmetrical property of a jet. As a result, a visual centerline cannot be clearly defined.

4.2. Time-mean tracer concentration field

The mean tracer field in the centerline longitudinal plane was obtained by time-averaging of the instantaneous images. Fig. 5(a) shows the time-averaged LIF image of a 30° dense jet ($Fr \approx 22$) as an illustration. The locus joining all local concentration maxima defines the jet trajectory. The mixing characteristics of an inclined dense jet can be clearly seen using concentration profiles at different parts of the jet trajectory. Fig. 5(b) shows representative transverse distribution of mean concentration with the non-dimensionalized concentration C/C_m plotted against dimensionless normal coordinate r/b_{gc}, where C_m = maximum concentration in jet cross-section, and b_{gc} is the radius defined by $C/C_m = 1/e = 0.37$. Close to the nozzle ('initial stage', $s/D \leq 20$, where s is the streamwise coordinate), the profiles can be well-approximated by a Gaussian distribution. Beyond around 20D, the profile for the inner (lower) half of the jet starts to depart from Gaussian whereas the outer (upper) half (negative r) remains Gaussian. This profile departure intensifies as the jet approaches the terminal rise, beyond which the profile seems to stabilize without further distortion ('developed stage'). The jet retains this 'stabilized' non-dimensionalized

Table 2

Summary of previous experimental studies; jet trajectory was measured in all studies and S_i in the table refers to the return point dilution unless otherwise specified.

Study	Method	Fr	Re	Dilution measured	Port height h_p
Present study	LIF/PIV	>10, <40	>2000	S_t, S_i	=10D
Papakostantis et al. (2011b)	Micro-conductivity	>18, <50	>6000	S_t, S_i	≥18.8D
Papakostantis et al. (2011a)	Visual	>7, <60	>1500	N/A	≥10D
Ferrari and Querzoli (2010)	LIF	>4.9, <40.2	=955	N/A	N/A
Shao and Law (2010)	LIF/PIV	>7, <32	>1390	S_t, S_i	≈4.1D (F series)
Kikkert et al. (2007)	LA, LIF	>27, <89	>2200	S_t, S_i (radially-integrated)	Source located at mid-height of a large tank
Nemlioglu and Roberts (2006)	3D-LIF	≈ 22	2245	S_i (at solid boundary)	N/A
Cipollina et al. (2005)	Visual	Mostly > 20, <216	>2500	N/A	N/A
Roberts et al. (1997)	LIF, micro-conductivity	≈ 20	>2789	S_i (at solid boundary)	≈8.2D
Roberts and Toms (1987)	Visual, fluorometry	> 12, <26	>1224	S_t, S_i	1D
Zeitoun et al. (1970)	Visual, fluorometry	>8, <53	>2700	S_t	∼38.5D
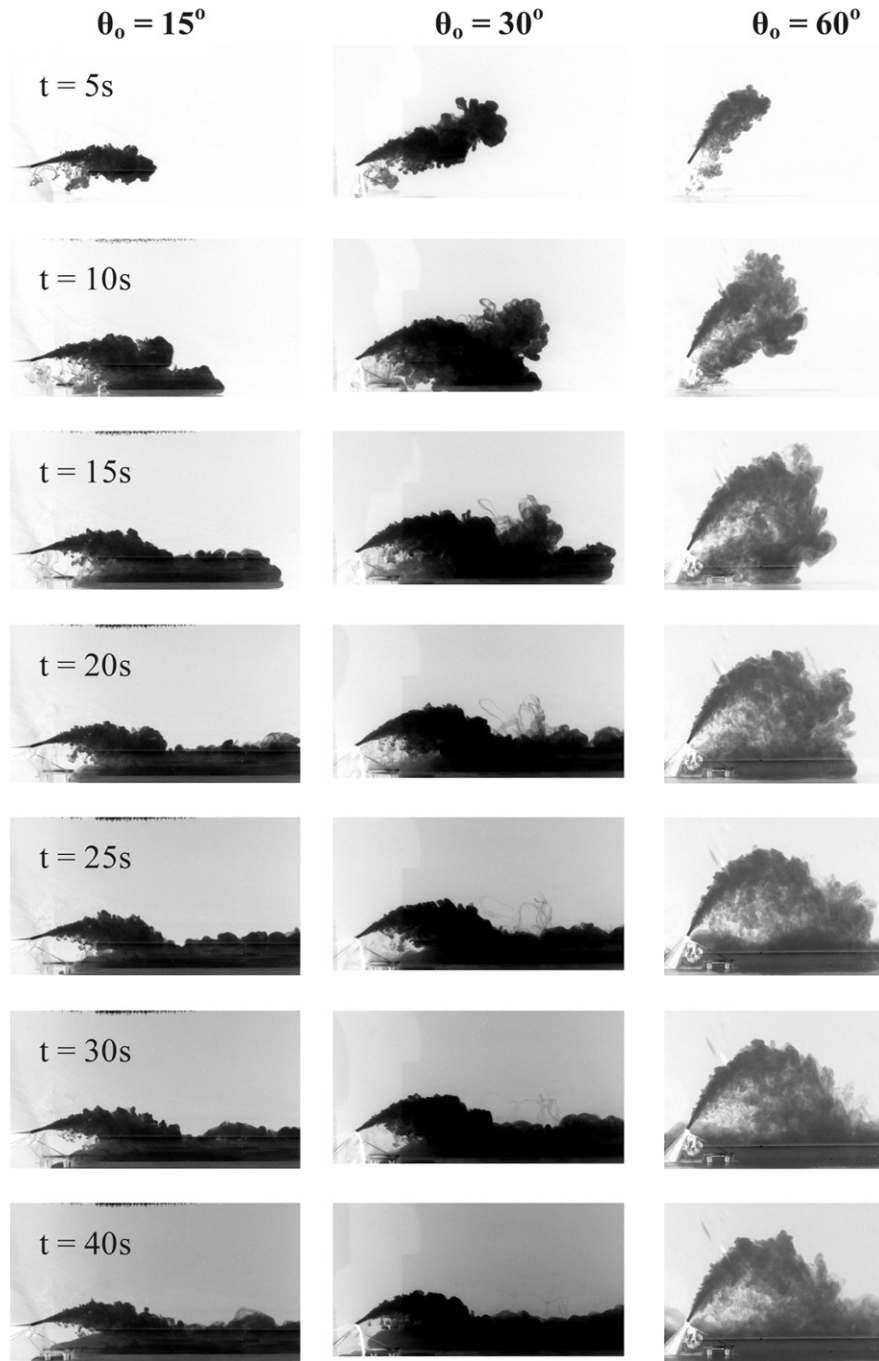
Fig. 4. Elevation view of dense jets at three jet discharge angles, $Fr = 16$.

profile for the rest of its trajectory before impinging onto the bottom. Throughout the entire trajectory, the upper half of the jet is always Gaussian with clear visual boundary. The profile distortion is a clear sign of detrainment — jet fluid is peeling off from the mean flow.

An implication of detrainment is that the negative buoyancy force calculated in the integral model will be larger than actual. Detrainment contributes an outflux of mass, momentum and buoyancy that is not modeled. As a result, the reduced negative buoyancy is not properly accounted for and the actual observed rise height will be higher than predicted.

The stabilization of concentration profile beyond terminal rise suggests that the buoyancy-driven instability vanishes on the descent of the dense jet from its maximum rise. The profile can be considered as composed of two parts; one part is axis-symmetric and Gaussian whereas the other part is indicative of detrainment (Fig. 6). Beyond the terminal point, the dense jet preserves its horizontal momentum while falling by gravity. Conceptually it can be thought of as a negatively buoyant jet (without detrainment) and a pure (negatively buoyant) plume resulting from the detrained mass flux.
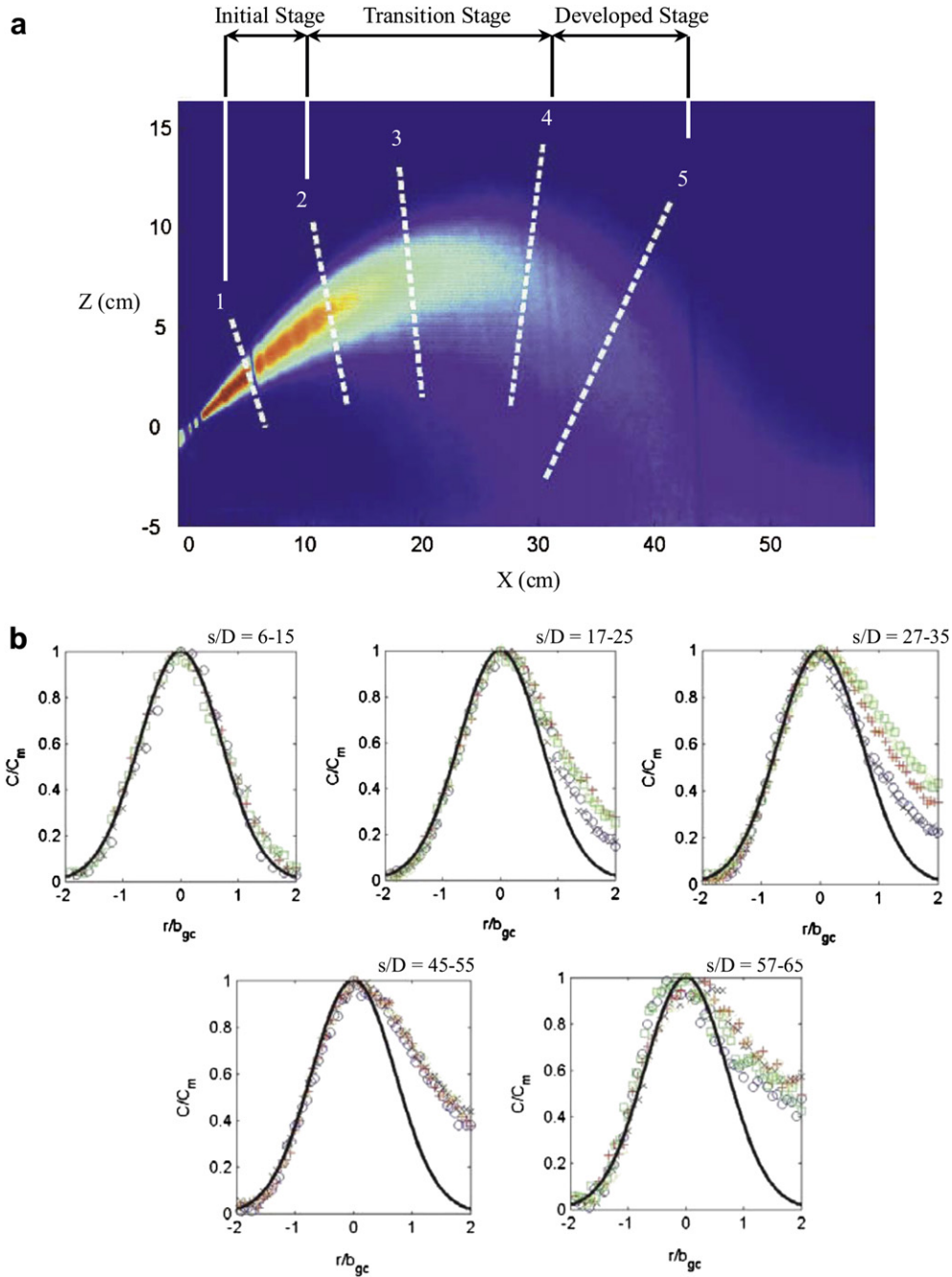
Fig. 5. Measured tracer concentration field of a 30° dense jet ($Fr = 21.8$) (a) time-averaged LIF image (b) representative cross-sectional profiles.

4.2.1. Growth of concentration jet width

The observation that the outer jet width is Gaussian is also supported by the jet growth rate. It was found that the concentration jet width grows at a rate equal to $b_{gc}/s = 0.1231$ (Fig. 7), which is essentially the same as the value of 0.125 reported by Chu (1996). The peeling off effect can also be quantified by inspecting the ratio R between the concentration jet width of the inner and outer edge (not shown). For the same 30° dense jet, R equals to one near the nozzle. Further downstream, it increases linearly to around two (i.e. 1.75–2) at the terminal rise where R remains unchanged thereafter. The resemblance of the jet width growth to that of a pure jet or

positively buoyant jet should not be a surprise. It is well-known that the spreading rate of a pure jet and a pure plume is approximately the same, although the entrainment coefficient of a plume is greater than that of a jet ($\alpha_p > \alpha_j$) by over 50 percent (see also Appendix A).

4.3. Jet trajectory and dilution

The jet centerline trajectory can be defined as the locus of transverse concentration maxima on the jet centerline longitudinal plane. Fig. 8 shows representative measured dimensionless centerline trajectory for inclined dense jets for three
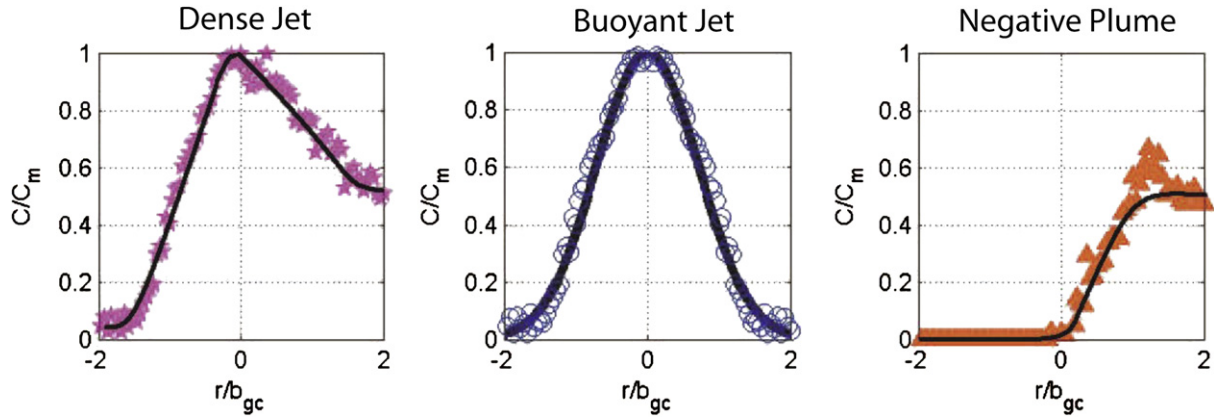
Fig. 6. Decomposition of concentration profiles after terminal rise.

discharge angles and $Fr \approx 26$. It is seen that the trajectory of an inclined dense jet is mainly affected by the jet discharge angle; for a given θ_o the trajectory lies within a narrow range before terminal rise. In the decent phase, there tends to be more scatter due to the buoyancy-instability. The corresponding predicted trajectory envelopes by VISJET for $Fr = 10$ and 40, covering the range of experiments, are also shown. The observed trajectory tends to be higher than the predicted due to the inability to account for detrainment in the model.

4.3.1. Visual terminal rise

For a positively buoyant jet in stagnant fluid, the visual boundary can be defined by the $0.25C_{max}$ concentration contour, which corresponds approximately to the radial position where turbulent intermittency γ is 0.5; it also corresponds to the jet boundary defined by the "top-hat" jet width (e.g. Chu

et al., 1999; Lee and Chu, 2003). In a dense jet, since the tracer distribution in the outer (upper) half is Gaussian and the outer jet width grows at the same rate as a positively buoyant jet, the $0.25C_{max}$ visual boundary definition is also adopted to determine the maximum visual rise Z_{max}. The predicted maximum rise height is defined as the sum of the vertical distance from source level to the jet's center of mass and the corresponding top-hat jet width B. Experiments of Chu (1996) have shown that the top-hat B, which is defined by the $0.25C_{max}$ (C_{mac} = cross-sectional concentration maximum) concentration contour, gives a good representation of the jet visual boundary. Fig. 9(a) shows the observed dimensionless maximum height of rise, Z_{max}/FrD as a function of the jet discharge Froude number Fr for six jet discharge angles $\theta_o = 15°, 30°, 38°, 45°, 52°, 60°$. It is seen that for a given jet angle, the dimensionless terminal rise has an additional dependence on Fr for small Fr, and approaches a constant for $Fr \geq 25$. The asymptotic dimensionless constant is about 10% greater than those of flows with $Fr \leq 25$. The same trend is predicted by VISJET (not shown).

Fig. 9(b) shows the observed asymptotic dimensionless centerline elevation and x-location at terminal rise (Z_c, X_c) as a function of jet angle θ_o. In general, the centerline elevation Z_c is under-estimated by VISJET by 10–15% due to
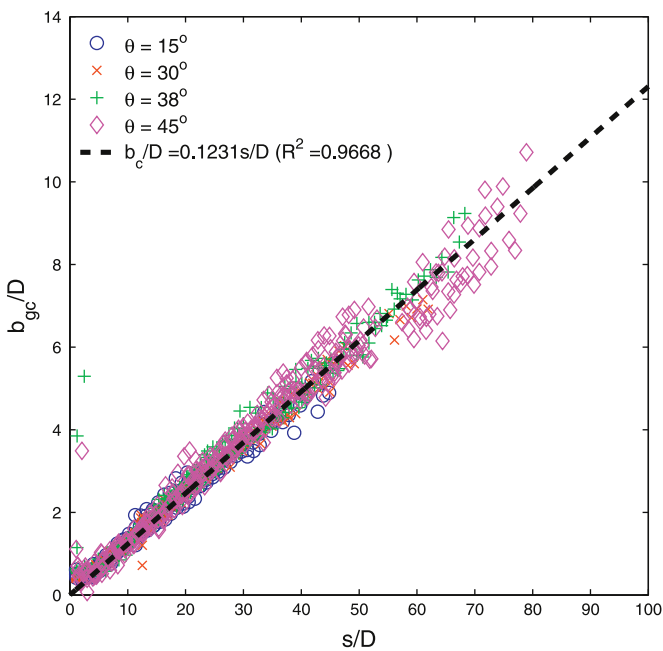
Fig. 7. Measured outer concentration jet width b_{gc} with streamwise distance.
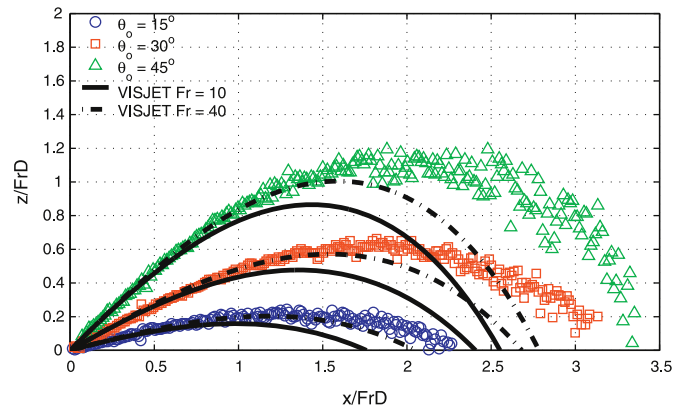
Fig. 8. Envelopes of measured centerline concentration trajectory of inclined dense jets.

detrainment. However, the relative insensitivity of the horizontal position of maximum height of rise (X_c) to discharge angle for $\theta_o \approx 30°-60°$ is well predicted. The discrepancy between predicted and observed X_c is relatively larger, around 25%; as the trajectory near the terminal rise is nearly horizontal, a small error in the predicted elevation would result in a relatively large error in x.

Fig. 10(a) shows the measured minimum dilution at terminal level as a function of jet densimetric Froude number Fr for different jet angles. It is seen that for Fr greater than about 20, the dimensionless dilution S_t/Fr approaches a constant which is approximately the same for different jet angles, with $S_t/Fr \approx 0.45$ for $\theta_o = 38°-60°$. For dense jets

without detrainment, $\theta_o = 15°$, the dilution constant is smaller, with $S_t/Fr \approx 0.27$. The impact dilution exhibits the same behavior, with a greater dilution constant of $S_i/Fr \approx 1.06$ for large Fr and for $\theta_o = 38°-60°$ (Fig. 10(b)).

The dilution ratio $R_s = S_i/S_t$ of each jet angle determined from experiment and the corresponding VISJET predictions are plotted in Fig. 10(c). The ratio is determined from dense jets with $Fr > 20$. Both experiments and predictions show that R_s increases with θ_o for $\theta_o = 15°-60°$ and the data agree favorably with predictions, with $S_i/S_t \approx 1.5-2.7$. Roberts and Toms (1987) gives $R_s = 2.7$ for the 60° dense jet which agrees with the predicted value of 2.75.

Fig. 11(a) shows the measured minimum dilution S_t at terminal height ($Fr = 20-40$) as a function of θ_o. For each jet angle, the sample mean of the data (dotted line) is shown along with all the data (open circles) and an error bar indicating one standard deviation from the mean. The 52° dense jet has the highest normalized dilution at terminal rise but there is, however, little difference in dilution for $\theta_o = 40°-60°$. This feature is predicted by VISJET but the values are under-estimated by about 30%. Fig. 11(b) shows the minimum return point ($z = 0$) dilution S_i for $Fr \geq 20$. Similarly, it was found that S_i/Fr is not sensitive to jet angle when $\theta_o \geq 38°$ although the dilution of 45° jets is somewhat higher. It generally takes on $S_i/Fr = 1.06$ which is a constant when $Fr \geq 20$.

Table 3 shows the comparison with past data of the measured dimensionless maximum and centerline rise heights (Z_{max}, Z_c), location of terminal rise (X_c) and impingement location (X_i − x-coordinate of dense jet when it returns to source level) whereas that for minimum dilution at terminal rise (S_t) and return level dilution (S_i) is shown in Table 4. The following points can be made:

- The present results cover a wider range of jet discharge angles than previously reported. For $\theta_o = 30°, 45°, 60°$, the measured terminal rise heights Z_{max} and centerline elevation Z_c are consistent with previous reported values. It is noted that measurements from both LIF and ordinary dye experiments are comparable with each other, supporting the choice of $0.25C_{max}$ as the visual boundary. In particular, our measurements of Z_{max} and Z_c for $\theta_o = 45°$, 60° are practically the same as the very recent results of Papakostantis et al. (2011a,b) who also experimented with additional non-vertical discharge angles of $\theta_o = 75°$, 80°, 85°.

- For the 60° jet Cipollina et al. (2005) reported a value of $Z_{max}/DFr = 2.32$; this seems to be notably higher than our value of 2.08, or the values by five other independent investigators with an average of 2.07. For the experiments of Kikkert et al. (2007), the maximum terminal rise of $Z_{max}/DFr = 2.43$ obtained from LIF measurements is also significantly higher than the value of 2.04 obtained using a light attentuation (LA) technique.

- The maximum height of rise is well-predicted by VISJET for small angles, $\theta_o = 15°$; however for larger angles the predicted maximum height of rise is lower than observed by 10−15% (as a result of detrainment which is not
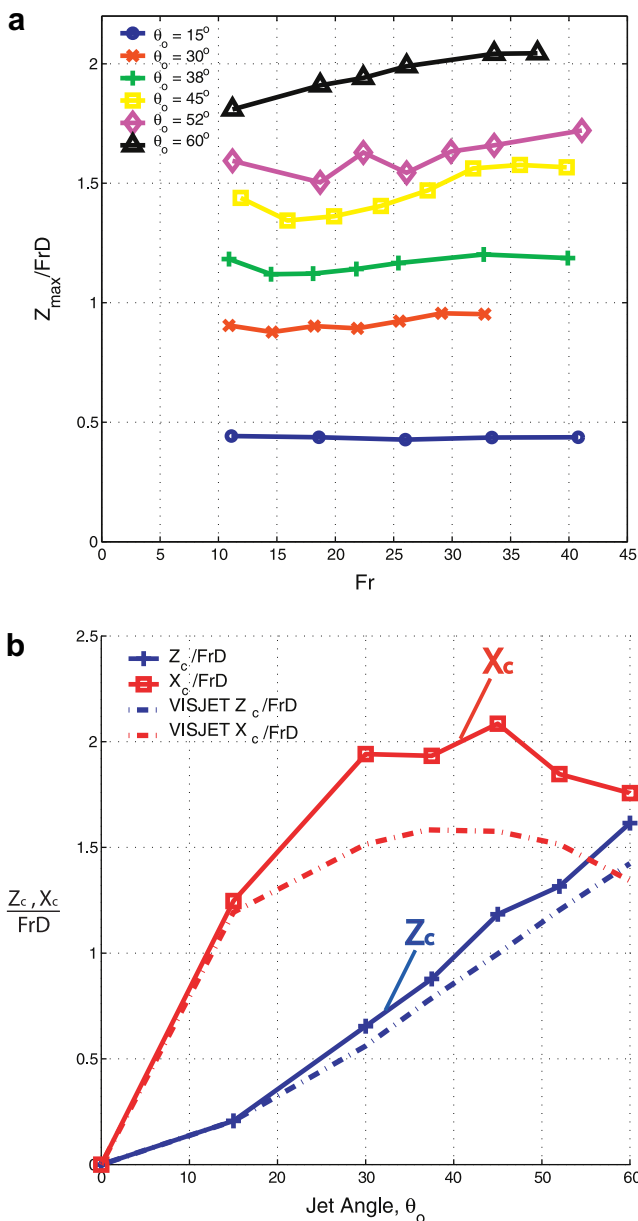
Fig. 9. Dense jet trajectories; (a) measured visual Z_{max} (jet boundary $= 0.25C_{max}$) against Fr; and (b) comparison of predicted and measured centerline location of jet trajectory at maximum rise (Z_c and X_c) vs jet angle.
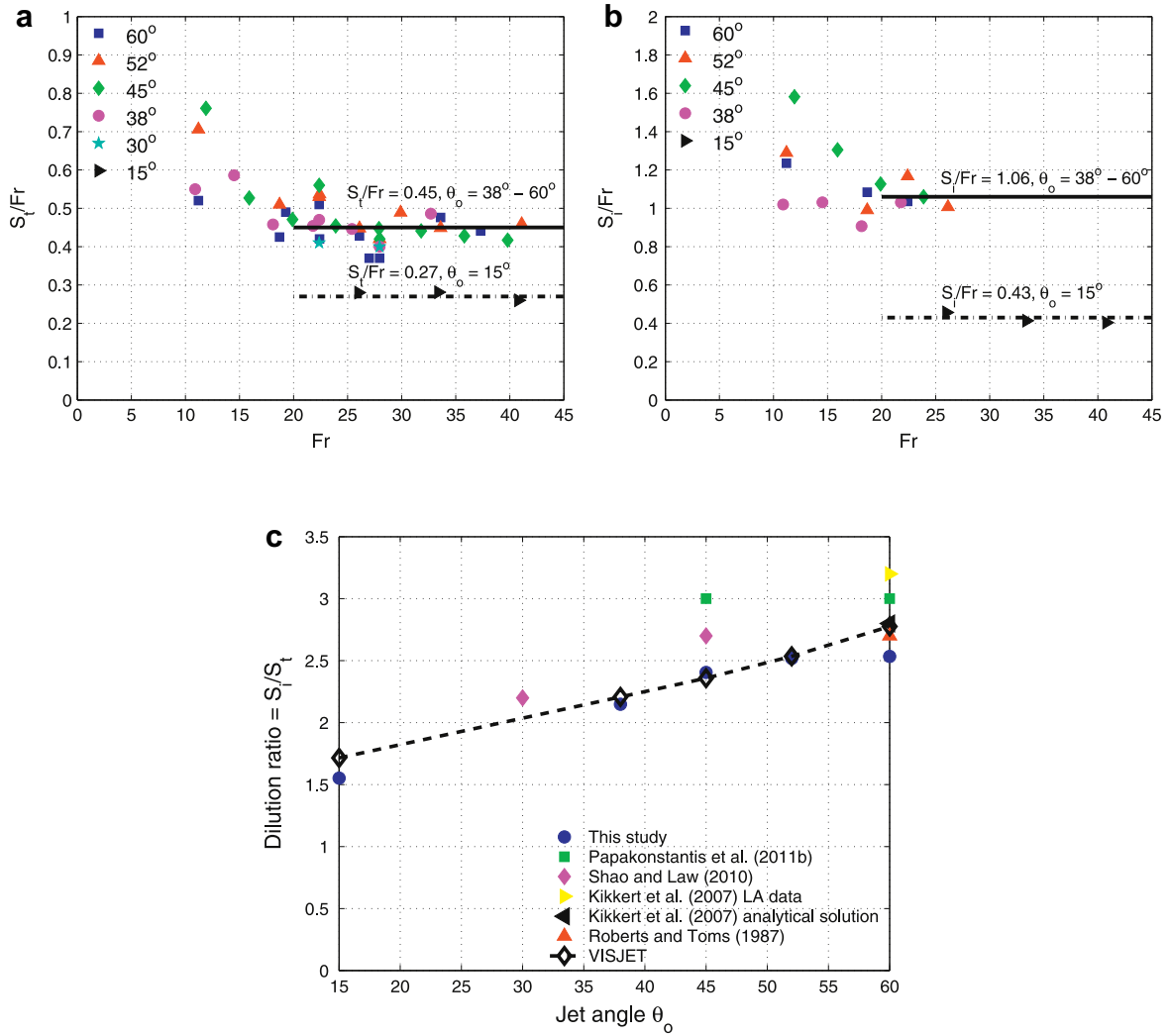
Fig. 10. Measured dilution of inclined dense jets: (a) minimum dilution at terminal rise S_t; (b) minimum dilution at return point S_i and (c) dilution ratio $R = S_i/S_t$ ($Fr > 20$) as a function of jet discharge angle.

modeled). The impingement location X_i is also under-predicted by about 10–15%.

• The measured dilution at terminal rise (for large Fr) is comparable with the data of Zeitoun et al. (1970) and Roberts and Toms (1987), but somewhat smaller than the recent results of Shao and Law (2010) and Papakostantis et al. (2011b). The present results provide the hitherto unavailable dilution constants over a wide range of jet
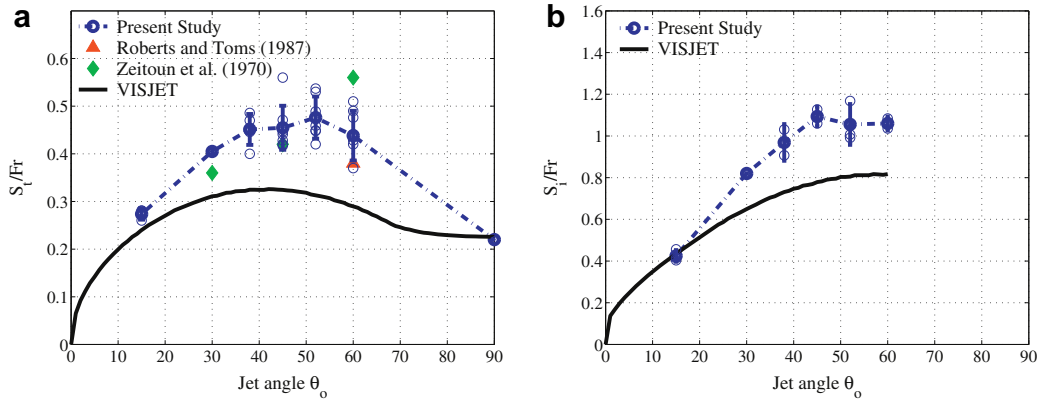
Fig. 11. Predicted and measured minimum dilution of inclined dense jets ($Fr > 20$) as a function of jet discharge angle: (a) dilution at terminal rise S_t (b) dilution at return point S_i

Table 3
Summary of experimental results with VISJET predictions; jet trajectory.

Jet Angle, θ_o	15°	30°	38°	45°	52°	60°
Jet trajectory						
Maximum terminal rise height			Z_{max}/FrD			
Present Study	0.44	0.95	1.20	1.58	1.69	2.08
Papakostantis et al. (2011b)	–	–	–	1.59	–	2.15
Papakostantis and Christodoulou (2008)	–	–	–	1.59	–	2.16
Shao and Law (2010)	–	–	–	1.47	–	–
Kikkert et al. (2007) (LIF/LA value)	0.52/0.52	1.17/1	–	1.61 (LA)	–	2.43/2.04
Cipollina et al. (2005)	–	1.08	–	1.61	–	2.32
Lindberg (1994)	–	–	–	1.56	–	2.16
Roberts et al. (1999)	–	–	–	–	–	1.93
Roberts and Toms (1987)	–	–	–	–	–	2.08
Zeitoun et al. (1970)	–	1.15	–	1.43	–	2.04
VISJET	0.44	0.86	1.10	1.33	1.55	1.78
Centerline rise height at Z_{max}			z_c/FrD			
Present Study	0.21	0.65	0.87	1.19	1.34	1.64
Papakostantis et al. (2011b)	–	–	–	1.17	–	1.68
Ferrari and Querzoli (2010)	–	–	–	1.19	–	1.67
Shao and Law (2010)	–	0.66	–	1.14	–	–
Kikkert et al. (2007) (LIF/LA value)	0.21/0.21	0.68/0.54	–	1.07 (LA)	–	1.71/1.46
Cipollina et al. (2005)	–	0.79	–	1.17	–	1.77
VISJET	0.21	0.56	0.77	1.00	1.20	1.42
Horizontal location at z_c			x_c/FrD			
Present Study	1.22	1.95	1.95	2.09	1.87	1.78
Shao and Law (2010)	–	1.54	–	1.69	–	–
Kikkert et al. (2007) (LIF/LA value)	1.47/1.22	1.84/1.75	–	1.81 (LA)	–	1.75/1.56
Cipollina et al. (2005)	–	1.95	–	1.80	–	1.42
VISJET	1.19	1.52	1.58	1.58	1.52	1.34
Horizontal distance from source to return point			X_i/FrD			
Present Study	2.41	3.18	3.19	3.34	2.87	2.84
Papakostantis et al. (2011b)	–	–	–	3.16	–	2.75
Ferrari and Querzoli (2010)	–	–	–	3.03	–	2.67
Shao and Law (2010)	–	3.00	–	3.33	–	–
Kikkert et al. (2007) (LIF/LA value)	2.53/2.13	3.40/3.07	–	3.20 (LA)	–	2.80 (LA)
Nemlioglu and Roberts (2006)	–	3.3	–	3.2	–	3.4 & 3.1
Cipollina et al. (2005)	–	3.03	–	2.82	–	2.25
Roberts et al. (1997)	–	–	–	–	–	2.40
VISJET	2.15	2.65	2.77	2.78	2.64	2.40

discharge angles. VISJET predictions of dilution are smaller than measured by about 30 percent; however the insensitivity of dilution to jet discharge angle in the range of $\theta_o = 38°–60°$ is well predicted.

Table 4
Summary of experimental results with VISJET predictions; minimum dilution.

Jet Angle, θ_o	15°	30°	38°	45°	52°	60°
Dilution						
Minimum dilution at terminal rise		S_t/Fr				
Present Study	0.27	0.40	0.45	0.45	0.47	0.44
Papakostantis et al. (2011b)	–	–	–	0.52	–	0.56
Shao and Law (2010)	–	0.62	–	0.46	–	–
Roberts and Toms (1987)	–	–	–	–	–	0.37
Zeitoun et al. (1970)	–	0.36	–	0.42	–	0.56
VISJET	0.24	0.31	0.32	0.32	0.31	0.29
Minimum dilution at X_i		S_i/Fr				
Present Study	0.43	0.82	0.99	1.09	1.10	1.07
Papakostantis et al. (2011b)	–	–	–	1.55	–	1.68
Shao and Law (2010)	–	1.45	–	1.26	–	–
Roberts and Toms (1987)	–	–	–	–	–	1.03
VISJET	0.41	0.64	0.73	0.77	0.81	0.83

- The minimum return level dilution S_i for $\theta_o = 60°$ is consistent with the data of Roberts and Toms (1987) and exhibits the same variation as S_t with jet discharge angle. Our data for S_i are notably lower than those reported by Papakostantis et al. (2011b); this may be related to the different experimental setup and measurement techniques near the impact point.

It is often suggested (Fischer et al. (1979)) that the terminal height of rise for different jet angles can be estimated based on the value at another jet angle by scaling the vertical component of the initial jet momentum:

$$Z_{max} \sim \frac{(M_o \sin\theta_o)^{\frac{3}{4}}}{F_o^{\frac{1}{2}}} \sim l_M (\sin\theta_o)^{\frac{3}{4}} \sim DFr(\sin\theta_o)^{\frac{3}{4}} \qquad (5)$$

This dimensionless relation states that the terminal rise of inclined dense jets with different θ_o can be scaled by the same constant. The predicted value solely based on the above extrapolation is significantly larger than measured values; for example, for 30° jet, based on the measured Z_c of the 60° jet,

Eq. (5) predicts $Z_c/(DFr)$ to be 1.07 compared to the measured value of 0.65. This shows that the dense jet behavior cannot be predicted purely using length scales. On the other hand, an integral model with the proposed variable entrainment hypothesis is able to predict this intricate variation of Z_c with jet angle. For example, Z_c of the 60° jet is 2.49 times that of 30° jet (1.64 vs 0.65, Table 3). VISJET predicts nearly the same value i.e. 1.42/0.56 = 2.54. Similar results can be found for any two other angles.

4.4. Jet centerline velocity

Fig. 12 shows the measured centerline velocity U_m with streamwise distance s from source to the return point of three selected cases of the 60° jet. There exists a potential core about 5D in length. The initial velocity decay (before Z_{max}) follows closely that of a pure jet, with $U_m \approx 7M_o^{1/2}s^{-1}$ (e.g. Fischer et al. (1979)). This is consistent with the results of 30° and 45° jets ($7 < Fr < 32$) by Shao and Law (2010) which gives a $s^{-1.1}$ centerline velocity decay for both jets. In a dense jet, U_m decays due to both jet spreading and negative buoyancy. It is therefore anticipated that it would decay faster than a pure momentum jet. The measurements however suggest that the effect of negative buoyancy is not significant in the decay of U_m, and seem to support the assumption of jet like behavior before maximum rise in the semi-empirical model of Kikkert et al. (2007).

4.5. Turbulence structure

The turbulence intermittency γ at a point is the portion of time in which that location is occupied by turbulence; it reflects the fluctuation of the turbulent and non-turbulent boundary. Fig. 13 shows the vertical profile of concentration intermittency of a 45° dense jet ($Fr = 19.8$). At locations close to the nozzle, the profile is the same as a pure jet in stagnant water; it is axis-symmetric, with a jet core of $\gamma = 1$ for $r/b_{gc} \le 0.75$ and $\gamma = 0.5$ at $r/b_{gc} \approx 1.2$. In a simple momentum jet, the jet edge as defined by a "top-hat" profile can be shown to correspond to

the location where the velocity intermittency is around 0.5 (e.g. Chu et al., 1999; Lee and Chu, 2003). On the other hand, the top-hat jet half-width is related to the Gaussian radius b_g by $B = \sqrt{2}b_g$. Hence the concentration at the jet edge is given by $C/C_m = \exp^{-(\sqrt{2}b_g/b_{gc})^2}$. With the concentration width $b_{gc} = \lambda b_g = 1.2b_g$, we have $C/C_m = \exp^{-2/1.44} = 0.249$. Hence the jet edge can be defined by the concentration boundary at $C/C_m \approx 0.25$; this appears to also apply for the upper half of the dense jet before terminal rise.

Further downstream, the inner edge profile is 'lifted' upwards, signifying the peeling off of jet fluid from mean flow. The outer edge is not affected and the radial position at which $\gamma = 0.5$ is still $1.2b_{gc}$. The intermittency profiles also collapse to a single curve for sections near or after the terminal rise, $s/D > 32$. The inner edge position where γ is equal to 0.5 is $r/b_{gc} = 2.1$ and $R = 2.1/1.2 = 1.75$, which is a constant after terminal rise.

Fig. 14(a) shows the concentration turbulent intensity C_{rms}/C_m at terminal rise Z_{max} for five jet angles: $\theta_o = 30°$, 38°, 45°, 52° & 60° ($Fr = 16-27$). These are vertical profiles cutting through the jet center plane at Z_{max}. All profiles are similar in shape; there is a peak at $r/b_{gc} = -0.76$, which is the outer jet edge; the normalized fluctuation at jet center $r = 0$ is around 0.2 and seems to decrease linearly from $r = 0$ toward the end of the tail ($r > 0$). Further, the peak value seemed to increase with jet angles; from 0.29 at 30° to 0.43 at 60°. The turbulence intensity along a horizontal transect through the level of C_m is also plotted (Fig. 14(b)). The profiles resemble those of a pure jet, with double peaks at $r/b_{gc} \approx \pm 0.76$; the measured turbulence intensity C_{rms}/C_m of 0.3 and 0.2 are considerably higher than the corresponding values (0.2 and 0.15) measured by Chu (1996) for a pure jet in stagnant ambient. All measurements are consistent with those in Papakostantis et al. (2011b) for $\theta_o \ge 45°$. Their measurements also suggest that the flow near the terminal rise is buoyancy-dominated; this is suggested by Eq. (4) that predicts α picking up the asymptotic plume value almost immediately after the terminal rise for $\theta_o \ge 45°$ (Fig. 2). Our
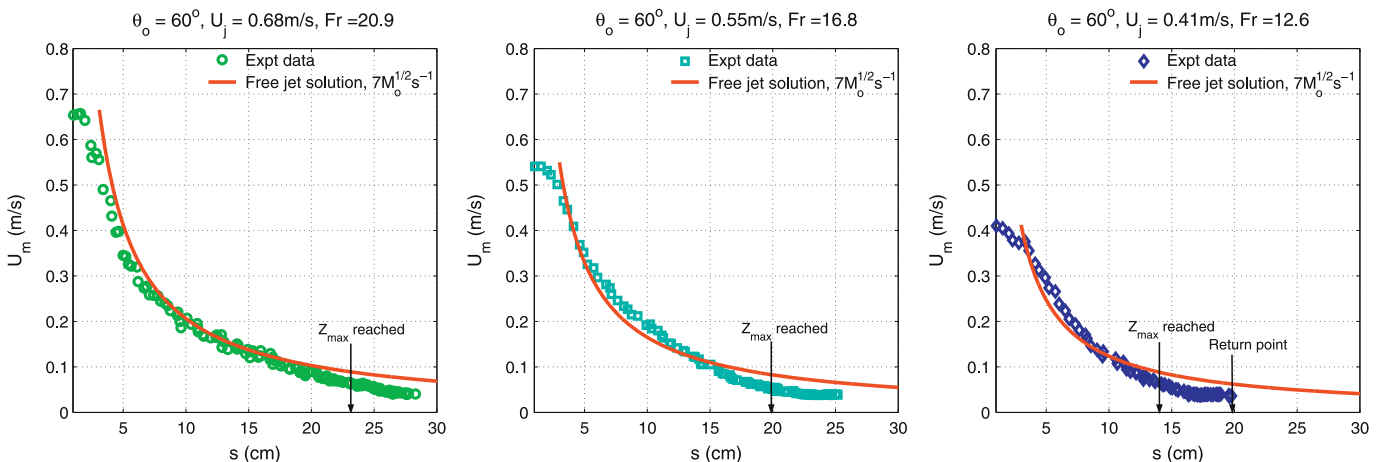
Fig. 12. Measured jet centerline velocity decay of 60° inclined dense jets.
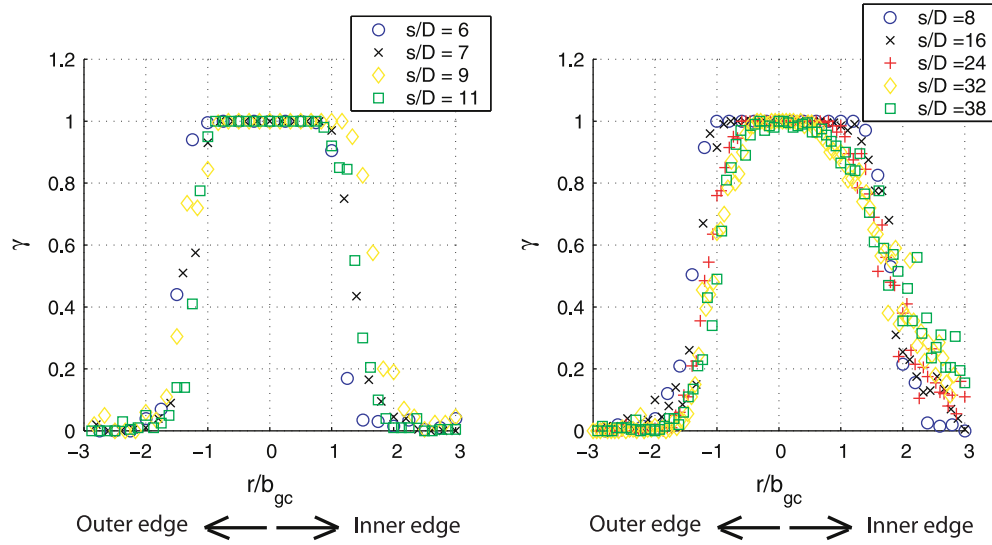
Fig. 13. Vertical profile of concentration intermittency in a 45° dense jet ($Fr = 19.8$).
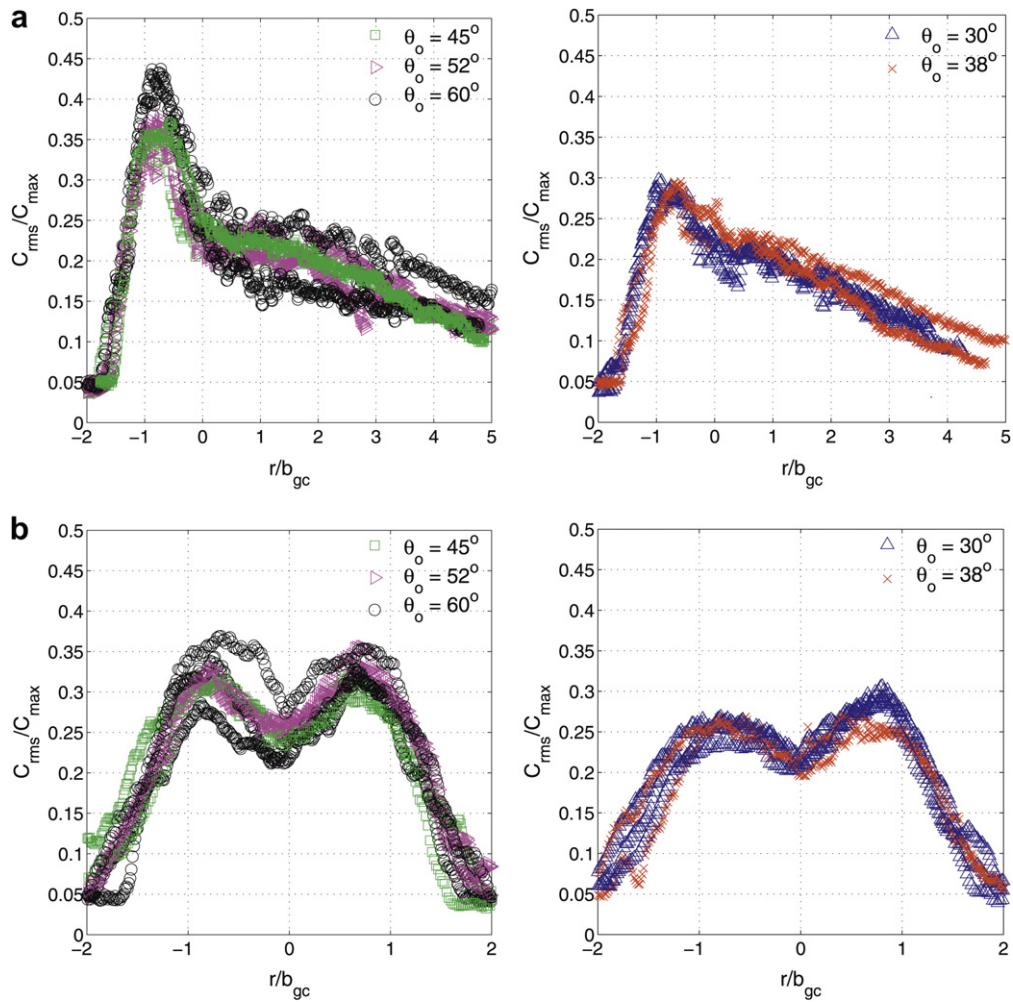
Fig. 14. Concentration turbulent fluctuation at terminal rise of inclined dense jets ($Fr = 17-28$): (a) vertical profile (b) horizontal profile.
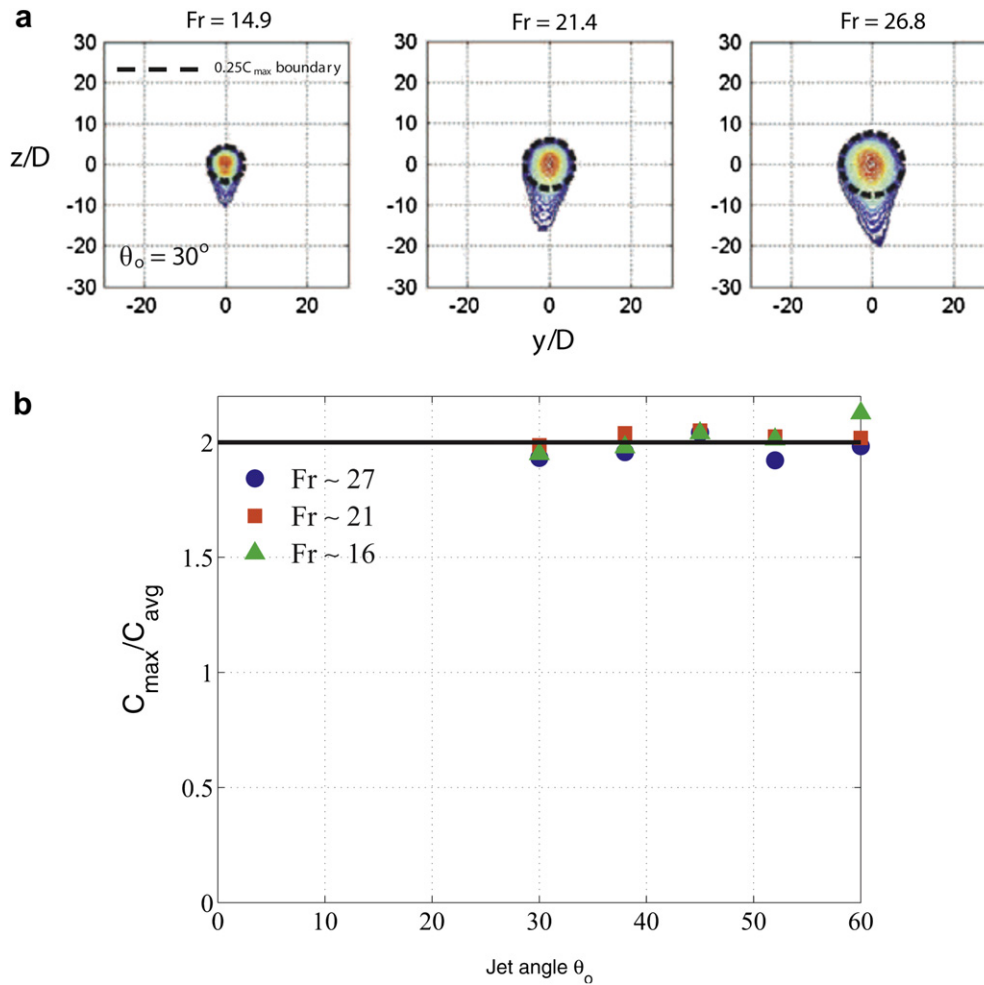
Fig. 15. Measured concentration at terminal rise of inclined dense jet: (a) Concentration contours of 30° dense jets; and (b) averaged concentration at terminal rise within the boundary defined by the jet concentration contour $0.25C_{max}$ as a function of jet discharge angle.

measurements for $\theta_o = 30°$ and $38°$ give a smaller maximum turbulent intensity at 0.3.

4.5.1. Cross-sectional concentration distribution at Z_{max}

The time-averaged concentration contours of five jet angles (at three Fr) were measured. Fig. 15(a) shows the results for 30° dense jets. The contours are scaled relative to C_m of the cross-section at an interval of $0.05C_{max}$. The visual jet boundary is defined by the $0.25C_{max}$ contour. A circle (in dotted lines) with radius ($= \sqrt{2}b_{gc}/1.2 = 1.17b_{gc}$) is drawn on the contour, where b_{gc} is based on the experimental growth rate ($b_{gc} = 0.1231$ s). The circumferences of the circles overlap nicely with the outermost $0.25C_{max}$ contour; the upper half of a dense jet is unaffected by detrainment, and is circular and symmetrical with respect to the vertical axis. As Fr increases, the elongated 'tail' at the lower edge lengthens as the jet rises higher. The detrainment is more profound for large jet angles. The average concentration within the $0.25C_{max}$ boundary, C_m/C_{avg}, is shown in Fig. 15(b). It can be seen that C_{avg} is around $0.5C_{max}$ for all 15 cross-sections.

5. Concluding remarks

A comprehensive experimental investigation has been carried out to study the detailed tracer concentration field of inclined dense jets with $Fr = 10–40$ and over a broad range of jet angles $\theta_o = 15°, 30°, 38°, 45°, 52°$ & $60°$. The experiments show that detrainment of jet fluid exists in dense jets. This is evident in both jet visualizations and time-mean concentration profiles. The upper half of the jet is gravitationally-stable and it moves as a coherent fluid parcel. The outer visual boundary can be defined by the $0.25C_{max}$ concentration contour and this is supported by the intermittency profiles and growth of outer concentration width b_{gc}. Jet centerline velocity measurements in the ascent phase and turbulence intensity profiles at terminal rise indicate that dense jets are in the jet-regime before terminal rise. Jet detrainment in the lower half is shown to be significant for $\theta_o > 15°$. Dilution measurements at terminal rise show the difference in dilution is small for $\theta_o = 38°–60°$ and the asymptotic dilution constant is $S_t/Fr = 0.45$. The return level dilution S_i is also not sensitive to jet angle for $\theta_o = 38°–60°$ and can be expressed as $S_i/Fr = 1.06$ for $Fr \geq 20$.

A general jet entrainment formulation that predicts the reduction of entrainment coefficient in dense jets is derived analytically and incorporated in a jet integral model to study the variation of jet properties with jet angle. The detrainment results in a smaller negative buoyancy and causes additional vertical mixing not accounted for by shear entrainment. Despite the neglect of jet detrainment, the theory gives reasonable predictions of the jet mixing properties — the predicted jet trajectory (e.g. Z_{max}) is underestimated by 10—15% and the associated dilution by 30%. However, the intricate variations of jet properties with jet angle is accurately predicted in particular the leveling off in normalized dilution for $\theta_o = 38°$—60°. It is also shown that while *ad hoc* reduction of entrainment coefficient to fit the observed jet trajectory can give better fit with the maximum rise data, the predicted dilution is unsatisfactory and cannot reflect the weak sensitivity of dilution to jet discharge angle.

Acknowledgment

Appendix A. General formulation of the entrainment coefficient

The entrainment hypothesis is often employed in an integral jet model for turbulent closure. The increase in jet volume flux along the unknown jet trajectory is expressed in terms of the local jet velocity and width via an entrainment coefficient α. The general dependence of the entrainment coefficient on the local jet densimetric Froude number is derived herein for a round buoyant jet. The approach was previously suggested for a positively buoyant jet (Fox, 1970) and had been explicitly developed for a plane buoyant jet (Jirka and Harleman, 1979). An original explicit derivation for a round buoyant jet is presented for completeness and to demonstrate clearly the significant reduction of entrainment for a dense jet.

Governing equations

Consider an arbitrarily inclined round positively buoyant jet in stagnant ambient (Fig. A.1) with $\rho_o < \rho_a$ by convention, where ρ_a, ρ_j are the ambient and jet discharge density respectively. The governing equations of motion can be written in a natural coordinate system (s, r), where s and r are the stream-wise and radial coordinates respectively; $u(s, r)$ and $v(s, r)$ are the axial and radial velocities. $g =$ gravitational accleration, and $\rho =$ fluid density. The local jet angle with the horizontal is defined as θ. By assuming small density differences, $\Delta\rho/\rho_a = (\rho_a - \rho)/\rho_a \ll 1$ and invoking the Boussinesq approximation (negligible density differences except in gravity terms), the Reynolds-averaged equations of the continuity and the axial momentum conservation equations can be written as:

$$\frac{\partial u}{\partial s} + \frac{1}{r}\frac{\partial rv}{\partial r} = 0 \tag{A.1}$$

$$u\frac{\partial u}{\partial s} + v\frac{\partial u}{\partial r} = g'\sin\theta - \frac{1}{r}\frac{\partial r\overline{u'v'}}{\partial r} \tag{A.2}$$

where u', v' are the turbulent velocity fluctuations, and $g' = g(\rho_a - \rho)/\rho_a$ is the local reduced gravity. The mechanical energy conservation Eq. (A.3) can be obtained by multiplying (A.1) by u^2 and (A.2) by u, followed by summing both equations.

$$\frac{\partial u^3}{\partial s} + \frac{1}{r}\frac{\partial ru^2v}{\partial r} = 2ug'\sin\theta - \frac{2u}{r}\frac{\partial r\overline{u'v'}}{\partial r} \tag{A.3}$$

Integral jet model

In the zone of established flow (ZEF) of the buoyant jet, the time-mean velocity profile $u(s, r)$ and concentration profile $c(s, r)$ are self-similar and can be approximated by Gaussian profiles (e.g. Fischer et al., 1979; Lee and Chu, 2003):

$$u(s, r) = u_m(s)e^{-\left(\frac{r}{b_s}\right)^2} \tag{A.4}$$

$$c(s, r) = c_m(s)e^{-\left(\frac{r}{\lambda b_s}\right)^2} \tag{A.5}$$

Fig. A.1. Schematic sketch of an inclined round buoyant jet in stagnant ambient.

where u_m and c_m are the centerline maximum velocity and tracer concentration; b_g and $b_{gc} = \lambda b_g$ are the characteristic velocity and concentration half-width where the velocity (concentration) has dropped to $1/e = 0.37$ of the centerline value. The spread of tracer is faster than momentum; experiments show the ratio of concentration to velocity half-width is given by $\lambda = b_{gc}/b_g \approx 1.2$. By virtue of self-similarity, the jet velocity and concentration field can be expressed in terms of the centerline variables u_m, c_m and the characteristic jet radius b_g. It can be shown that the jet volume flux $Q = \int u dA = \int u 2\pi r dr = \pi u_m b_g^2$, and the jet momentum flux $M = \int u^2 dA = \int u^2 2\pi r dr = (\pi/2)u_m^2 b_g^2$. By assuming a linear equation of state, the density difference, is linearly proportional to the scalar concentration c, $\Delta\rho = \rho_a - \rho \sim c$; hence the local reduced gravity $g' = (\Delta\rho(s,r)/\rho_a)g$ is also Gaussian:

$$g'(s,r) = g'_m(s)e^{-\left(\frac{r}{\lambda b_g}\right)^2} \tag{A.6}$$

The continuity Eq. (A.1) is transformed by multiplying by $2\pi r dr$ throughout and integrating across the jet from $r = 0$ to ∞.

$$\frac{\partial}{\partial s}\int_0^\infty u 2\pi r dr = -\int_0^\infty \frac{1}{r}\frac{\partial rv}{\partial r}2\pi r dr = -2\pi[rv]_0^\infty$$
$$\frac{du_m b_g^2}{ds} = 2b_g \alpha u_m \tag{A.7}$$

The term $-2\pi[rv]_0^\infty$ is the entrainment inflow into the jet; rv is replaced by the product of b_g and an entrainment velocity v_e. The entrainment velocity v_e at $r = b_g$ is assumed to be proportional to the centerline jet velocity, where the proportionality constant α is defined as the entrainment coefficient:

$$v_e = \alpha u_m \tag{A.8}$$

By adding $u[(\partial u/\partial s) + (1/r)(\partial rv/\partial r)] = 0$ to the axial momentum equation, (A.2), the momentum conservation can be expressed in integral form as:

$$\int_0^\infty \left[\frac{\partial u^2}{\partial s} + \frac{1}{r}\frac{\partial ruv}{\partial r}\right]2\pi r dr = \int_0^\infty \left[g'\sin\theta - \frac{1}{r}\frac{\partial r\overline{u'v'}}{\partial r}\right]2\pi r dr$$
$$\frac{du_m^2 b_g^2}{ds} = 2\lambda^2 b_g^2 g'_m \sin\theta \tag{A.9}$$

Eq. (A.9) shows that the increase in jet momentum flux is generated by the local buoyancy force due to the distribution of density difference g'.

The mechanical energy conservation Eq. (A.3) can be similarly integrated over the entire jet cross-section.

$$\int_0^\infty \left[\frac{\partial u^3}{\partial s} + \frac{1}{r}\frac{\partial ru^2v}{\partial r}\right]2\pi r dr = \int_0^\infty \left[2ug'\sin\theta - \frac{2u}{r}\frac{\partial r\overline{u'v'}}{\partial r}\right]2\pi r dr \tag{A.10}$$

The Reynolds stress, $\overline{u'v'}$, is also assumed to be self-similar and can be written as $u_m^2 f(r/b)$ where f is an unknown function invariant to s and r.

The 1st term on the left hand side (L.H.S) of Eq. (A.10) $\partial u^3/\partial s$ – represents the transport of mean flow energy in the axial direction.

$$\int_0^\infty \frac{\partial u^3}{\partial s}(2\pi r)dr = \frac{\pi}{3}\frac{du_m^3 b_g^2}{ds}$$

The 2nd term on the L.H.S vanishes upon integration. As $r\to\infty$, $2\pi rv$ = entrainment flux is finite, but $u\to0$; when $r\to0$, u is finite and $v\to0$ by symmetry.

The 1st term on R.H.S $2 ug'\sin\theta$ – represents the gravitational force acting on the flow.

$$\int_0^\infty 2ug'\sin\theta(2\pi r)dr = \frac{\pi\lambda^2}{1+\lambda^2}2\sin\theta u_m g'_m b_g^2$$

The 2nd term on R.H.S $(2u/r)(\partial r\overline{u'v'}/\partial r)$ – represents the interaction of mean flow and turbulent shear stress.

$$\int_0^\infty \frac{2u}{r}\frac{\partial r\overline{u'v'}}{\partial r}2\pi r dr = 4\pi u_m^3 I_1 b_g$$

where I_1 is the shape integral defined as $I_1 = \int_0^\infty e^{-(r/b_g)^2}\partial[(r/b_g)f(r/b_g)]/\partial r$. It represents the interaction between mean flow velocity u and shear stress $\overline{u'v'}$.

The integral form of the mechanical energy equation can then be written as:

$$\frac{\pi}{3}\frac{du_m^3 b_g^2}{ds} = \frac{\pi\lambda^2}{1+\lambda^2}2\sin\theta u_m g'_m b_g^2 - 4\pi u_m^3 I_1 b_g \tag{A.11}$$

The L.H.S of Eq. (A.11) can be decomposed into the difference of two parts according to the following identity:

$$\frac{du_m^3 b_g^2}{ds} = 2u_m \frac{d}{ds}\left(u_m^2 b_g^2\right) - u_m^2\frac{d}{ds}\left(u_m b_g^2\right)$$

With this identity, and using Eq. (A.7) and Eq. (A.9), Eq. (A.11) can be written as:

$$\frac{4\pi\lambda^2 b_g^2 g'_m \sin\theta u_m}{3} - \frac{2\pi}{3}u_m^3 b_g \alpha = \frac{\pi\lambda^2}{1+\lambda^2}2\sin\theta u_m g'_m b_g^2 - 4\pi u_m^3 I_1 b_g \tag{A.12}$$

Defining the local densimetric Froude number as $Fr_L = u_m/\sqrt{(\Delta\rho_m/\rho_a)gb_g} = u_m/\sqrt{g'_m b_g}$, the entrainment relation between α and Fr_L for a round buoyant jet can be obtained as

$$\alpha = 6I_1 + \left(2 - \frac{3}{1+\lambda^2}\right)\sin\theta\frac{\lambda^2}{Fr_L^2} \tag{A.13}$$

It can be seen that the entrainment coefficient is predicted to be a function of the local jet angle θ and the local jet

densimetric Froude number Fr_L, and can be cast in a general form as:

$$\alpha = C_1 + C_2 \frac{\sin\theta}{Fr_L^2} \tag{A.14}$$

where C_1 and C_2 are constants. The constants C_1 and C_2 can be determined from well-established data of entrainment coefficient for the limiting cases of a pure jet ($\alpha_j = 0.057$) and a pure plume ($\alpha_p = 0.085$). It is well known that the entrainment coefficient of a plume is greater than that of a jet, $\alpha_p > \alpha_j$. As $Fr_L \to \infty$ (for a pure momentum jet), $\alpha \to \alpha_j$,

$$C_1 = \alpha_j$$

It can be shown that all buoyant (positively) jets tend to be plumes far away from the source (e.g. Lee and Chu, 2003). As the jet trajectory becomes vertical, $\theta \to 90°$, $Fr_L \to Fr_p$, which is the asymptotic densimetric Froude number for a plume, $\alpha \to \alpha_p$. For a round plume, it can be shown that $Fr_p = \sqrt{5\lambda^2/4\alpha_p} = 4.6$ (Lee and Chu, 2003, pp. 97–99), and

$$\alpha_p = \alpha_j + \frac{C_2}{Fr_p^2} \tag{A.15}$$
$$C_2 = (\alpha_p - \alpha_j)Fr_p^2$$

Substituting C_1 and C_2 into Eq. (A.16), the general formulation for the entrainment coefficient is obtained.

$$\alpha = \alpha_j + (\alpha_p - \alpha_j)\sin\theta\frac{Fr_p^2}{Fr_L^2} \tag{A.16}$$

It should be noted that although a positively buoyant jet is assumed by convention, $\rho < \rho_a$, the general theory is valid for $\rho > \rho_a$. In particular, for a dense jet with $\rho_o > \rho_a$, $Fr_L^2 < 0$ and Eq. (A.16) suggests the second term is negative and can result in the reduction of the entrainment coefficient to below the value of a simple jet, $\alpha < \alpha_j$.

Appendix B. Comparison between predictions of alternative entrainment formulations

The generality of Eq. (4) can be best illustrated by comparing the predictions of jet properties using several variants of the entrainment hypothesis with the dense jet measurements. Three different hypotheses are tested using the JETLAG/VISJET model:

H1 Assumed pure jet behavior, $\alpha = \alpha_j = 0.057 = $ constant
H2 $\alpha = f(\theta, Fr_L)$, Eq. (4)
H3 $\alpha = f(\theta, Fr_L)$, Eq. (4) with an artificially reduced $\alpha_j = 0.0403$

Fig. B.1(a) shows the predicted Z_{max} as a function of jet discharge angle for the three entrainment hypotheses. It can be seen that by artificially setting $\alpha_j = 0.0403$ (H3), the prediction matches closely with measured values. On the other hand, the prediction with the general hypothesis H2, Eq. (4), underestimates the maximum rise by around 10–15% for $\theta \geq 30°$ – due to the inability to model detrainment. The predicted terminal rise by assuming a pure jet (H1) is graphically indistinguishable from that of H3 reflecting the jet-like character of the dense jet before terminal rise. Similar statements can be made for the predicted and measured longitudinal distance of the return point (not shown).

Fig. B.1(b) shows the predicted return point minimum dilution S_i (obtained from the average dilution $\bar{S}$ as $\bar{S}/1.7$) as a function of jet discharge angle. It can be seen that only hypothesis H1 and H2 predict the observed leveling off of S_i/Fr for $\theta_o \geq 40°$ and Eq. (4) gives the closest agreement with measurements. By artificially reducing α_j, H3 does predict the jet trajectory more satisfactorily but the dilution is poorly predicted; it also fails to predict the weak sensitivity of the dilution to jet discharge angle. This shows the fundamental inconsistency of the artificial adjustment of entrainment coefficient to fit data of dense jet trajectory.

(a)

(b)
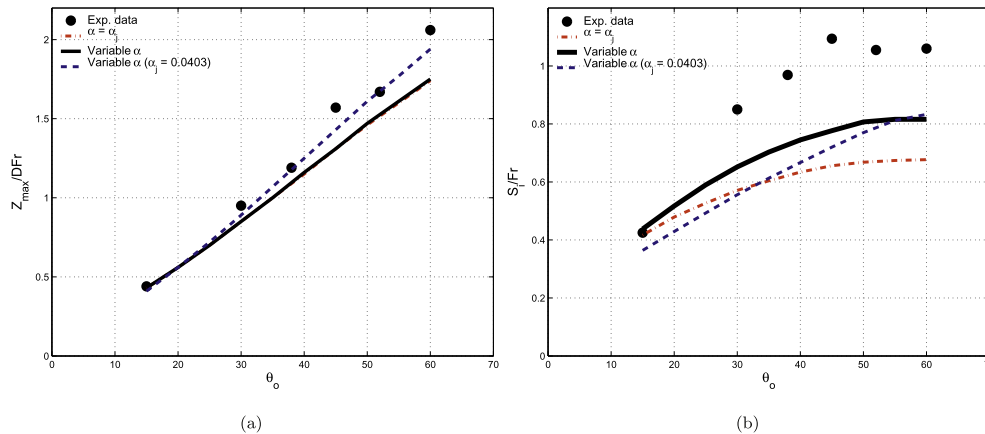
Fig. B.1. Predictions and measurements (this study, in black circles) (a) visual terminal rise Z_{max} and (b) return point minimum dilution $S_i = \bar{S}/1.7$.

References

Abraham, G., 1967. Jets with negative buoyancy in homogenous fluid. Journal of Hydraulic Research 5 (4), 235−248.

Anwar, H.O., 1969. Behavior of buoyant jet in calm fluid. Journal of the Hydraulic Division, ASCE 95, 1289−1303. HY4, Proc. paper 6688.

Cederwall, K., 1968. Hydraulics of Marine Wastewater Disposal. Hydraulics Div., Chalmers Institute of Technology, Sweden. Report No.42.

Chu, P.C.K., 1996. Mixing of turbulent advected line puffs. Ph.D. thesis, Dept of Civil and Structural Engineering, the University of Hong Kong, 222p.

Chu, P.C.K., Lee, J.H.W., Chu, V.H., 1999. Spreading of a turbulent round jet in coflow. Journal of Hydraulic Engineering, ASCE 125 (2), 193−204.

Cipollina, A., Brucato, A., Grisafi, F., Nicosia, S., 2005. Bench-Scale investigation of inclined dense jets. Journal of Hydraulic Engineering, ASCE 131 (11), 1017−1022.

Ferrari, S., Querzoli, G., 2010. Mixing and re-entrainment in a negatively buoyant jet. Journal of Hydraulic Research 48 (5), 632−640.

Fischer, H.B., List, E.J., Koh, R.C.Y., Imberger, J., Brooks, N.H., 1979. Mixing in Inland and Coastal Waters. Academic Press.

Fox, D.G., 1970. Forced plume in a stratified fluid. Journal of Geophysical Research 75, 6818−6835.

Jirka, G.H., Harleman, D.R.F., 1979. Stability and mixing of a vertical plane buoyant jet in confined depth. Journal of Fluid Mechanics 94 (2), 275−304.

Jirka, G.H., 2004. Integral model for turbulent buoyant jets in unbounded stratified flows. Part I: the single round jet. Environmental Fluid Mechanics 4, 1−56.

Jirka, G.H., 2008. Improved discharge configurations for brine effluents from desalination plants. Journal of Hydraulic Engineering, ASCE 134 (1), 116−120.

Kikkert, G.A., Davidson, M.J., Nokes, R.I., 2007. Inclined negatively buoyant discharges. Journal of Hydraulic Engineering, ASCE 133 (5), 545−554.

Lai, C.C.K., 2010. Mixing of inclined dense jets. M.Phil. thesis, Dept of Civil Engineering, the University of Hong Kong, 132p.

Lee, J.H.W., Cheung, V., 1990. Generalized Lagrangian model for buoyant jets in a current. Journal of Environmental Engineering, ASCE 116 (6), 1085−1106.

Lee, J.H.W., Cheung, V., Wang, W.P., Cheung, S.K.B., 2000. Lagrangian modeling and visualization of rosette outfall plumes. In: Proc. Hydroinformatics 2000, Iowa, July 23−27, 2000, (CDROM).

Lee, J.H.W., Chu, V.H., 2003. Turbulent Jets and Plumes: a Lagrangian Approach. Kluwer Academic Publishers, The Netherlands.

Lindberg, W.R., 1994. Experiments on negatively buoyant jets, with and without crossflow. In: Davies, P.A., Neves, M.J. (Eds.), Recent research advances in the fluid mechanics of turbulent jets and plumes. Kluwer, Dordrecht, The Netherlands, pp. 131−145.

Milione, M., Zeng, C., 2008. The effects of temperature and salinity on population growth and egg hatching success of the tropical calanoid copepod, Acartia sinjiensis. Aquaculture 275, 116−123.

Morton, B.R., Taylor, G.I., Turner, J.S., 1956. Turbulent gravitational convection from maintained and instantaneous sources. Proceedings of the Royal Society A234, 1−23.

Nemlioglu, S., Roberts, P.J.W., 2006. Experiments on dense jets using three-dimensional laser-induced fluorescence (3DLIF). Proceedings of the 4th International Conference on Marine Waste Water Disposal and Marine Environment.

Papanicolaou, P.N., Papakostantis, I.G., Christodoulou, G.C., 2008. On the entrainment coefficient in negatively buoyant jets. Journal of Fluid Mechanics 614, 447−470.

Papakostantis, I.G., Christodoulou, G.C., Papanicolaou, P.N., 2011a. Inclined negatively buoyant jets 1: geometrical characteristics. Journal of Hydraulic Research 49 (1), 3−12.

Papakostantis, I.G., Christodoulou, G.C., Papanicolaou, P.N., 2011b. Inclined negatively buoyant jets 2: concentration measurments. Journal of Hydraulic Research 49 (1), 13−22.

Papakostantis, I.G., Christodoulou, G.C., 2008. Discussion on "Inclined negatively buoyant discharges" by G.A. Kikkert, M.J. Davidson, and R.I. Nokes. Journal of Hydraulic Engineering, ASCE 134 (12), 1782−1784.

Roberts, P.J.W., Toms, G., 1987. Inclined dense jets in flowing current. Journal of Hydraulic Engineering, ASCE 113 (3), 323−341.

Roberts, P.J.W., Ferrier, A., Daviero, G., 1997. Mixing in inclined dense jets. Journal of Hydraulic Engineering, ASCE 123 (8), 693−699.

Roberts, P.J.W., Ferrier, A., Daviero, G., 1999. Closure of "Mixing in inclined dense jets" by Roberts et al. (1997). Journal of Hydraulic Engineering, ASCE 125 (3), 318−319.

Shao, D., Law, A.W.K., 2010. Mixing and boundary interactions of 30° and 45° inclined dense jets. Environmental Fluid Mechanics 10, 521−553.

Zeitoun, M.A., Reid, R.O., McHilhenny, W.F., Mitchell, T.M., 1970. Model Studies of Outfall System for Desalination Plants. Research and Development Progress Rep. 804. Office of Saline Water, U.S. Dept of Interior, Washington, D.C.